Kinematics and Source Zone Properties of the 2004 Sumatra-Andaman Earthquake and Tsunami: Nonlinear Joint Inversion of Tide-Gage, Satellite Altimetry and GPS data

S. Lorito, A. Piatanesi, V. Cannelli, F. Romano, and D. Melini

Istituto Nazionale di Geofisica e Vulcanologia, Department of Seismology and Tectonophysics, Via di Vigna Murata 605, 00143 Rome, Italy

Running title: Sumatra 2004 joint inversion

Corresponding author: Stefano Lorito,
Istituto Nazionale di Geofisica e Vulcanologia, Sezione di Sismologia e Tettonofisica, Via di Vigna Murata 605, 00143 Rome, Italy
E-mail: stefano.lorito@ingv.it
Phone:+390651860584
Fax:+390651860507

submitted to *JGR Solid Earth*, July, 2008
Revision, March 2009

Abstract

We (re)analyzed the source of the 26 December 2004 Sumatra-Andaman earthquake and tsunami through a nonlinear joint inversion of an in-homogeneous dataset made up of tide-gages, satellite altimetry, and far-field GPS recordings. The purpose is two-fold: (1) the retrieval of the main kinematics rupture parameters (slip, rake, rupture velocity); (2) the inference of the rigidity of the source zone. We independently estimate the slip from tsunami data and the seismic moment from geodetic data, so to derive the rigidity. Our results confirm that the source of the 2004 Sumatra-Andaman earthquake has a complex geometry, constituted by three main slip patches, with slip peaking at ~30 meters in the Southern part of the source. The rake direction rotates counter-clockwise at North, according to the direction of convergence along the trench. The rupture velocity is higher in the deeper than in the shallower part of the source, consistently with the expected increase of rigidity with depth. It is also lower in the Northern part, consistently with known variations of the incoming plate properties and shear velocity. Our model features a rigidity (20-30 GPa), that is lower than PREM average for the seismogenic volume [*Dziewonski and Anderson*, 1981]. The source rigidity is one of the factors controlling the tsunamigenesis: for a given seismic moment, the lower the rigidity, the higher the induced seafloor displacement. The general consistence between our source model and previous studies supports the effectiveness of our approach to the joint inversion of geodetic and tsunami data for the rigidity estimation.

1. Introduction

The 26 December 2004 M=9.1-9.3 [*Stein and Okal*, 2005; *Chlieh et al.*, 2007] earthquake struck the Sumatra-Andaman region and generated a huge tsunami. This was the most devastating and deadly seismic event occurred during the last centuries, causing more than 250,000 fatalities and spreading destruction along the coasts of the whole Indian Ocean.

The 2004 Sumatra event produced the biggest and most complete ever dataset for a great earthquake and its associated tsunami. For example, the associated tsunami wave has been recorded by several tide-gages in the Indian Ocean, as well as in both the Pacific and Atlantic Oceans [*Merrifield et al.*, 2005; *Titov et al.,* 2005; *Dragani et al.,* 2006; *Joseph et al.,* 2006; *Nagarajan et al.*, 2006; *Obura,* 2006; *Rabinovich et al.*, 2006; *Tanioka et al.*, 2006b; *Tsuji et al.* 2006; *Rabinovich and Thomson*, 2007; *Thomson et al.,* 2007].

Since then, many researchers all over the world have been studying this earthquake, as testified by at least four special issues on scientific journals [*Gu,* 2006; *Tanioka et al.*, 2006a; *Bilek et al.*, 2007; *Satake et al.,* 2007], and by a number of other papers. In particular, some researchers investigate the (kinematical) properties of the source of this earthquake. Its unusual size (moment, extent, duration) made this earthquake a real benchmark for the refinement of inversion methods, based on many different types of geophysical data. In this paper we have used both tsunami (as recorded by tide-gages and altimeter satellites) and geodetic data.

Tanioka et al. [2006b] and *Piatanesi and Lorito,* [2007] propose models of the slip distribution and average rupture velocity of the seismic source based on the inversion of tide-gage records of the 2004 tsunami in the Indian Ocean. *Hirata et al.* [2006] estimate the tsunami source model by inverting the altimetry signals recorded by two satellites, which flew above the Indian Ocean about two hours after the earthquake. *Fujii and Satake* [2007] combine tide-gage and three satellite recordings of the tsunami and infer the rupture characteristics through a joint inversion of the two datasets.

On the other hand, geodetic data have been inverted by a number of authors to constrain the seismic source properties. *Banerjee et al.,* [2005], *Catherine et al.*, [2005], *Vigny et al.,* [2005], and *Hashimoto et al.* [2006] use far-field GPS recordings; *Gahalaut et al.* [2006] use near-field GPS recordings; *Subarya et al.* [2006], and *Banerjee et al.* [2007] use both GPS

records in the near-field and vertical motion of coral reefs. *Chlieh et al.* [2007] and *Pietrzak et al.* [2007] combine near- to far-field GPS and coral reefs data, and successively validate their results against tsunami data. A joint inversion of GPS and seismic data is performed by *Rhie et al.* [2007].

Nevertheless, there are still some open questions about the details of the source process solutions proposed by different authors. The situation is somewhat ameliorated when refining the modeling strategies, as demonstrated by the most recent inversions. *Sladen and Hébert* [2008] use an up-to-date structural model of the causative fault. *Hoechner et al.* [2008] reconciliate near- and far-field modeling of the coseismic displacement, by using a continental Earth's layering rather than an oceanic one.

In the present work, we combined tsunami and geodetic datasets in a joint inversion. Our inhomogeneous dataset is made up of (1) tide-gages, (2) satellite altimetry, and (3) far-field GPS recordings. In light of the results described above, we adopted a fault geometry with variable strike and dip [*Subarya et al.*, 2006]. We modeled the coseismic displacement at GPS sites by taking into account Earth's sphericity and layering, due to their importance in the far-field [*Banerjee et al.,* 2005]. However, we conservatively decided not to include near-field (campaign) GPS recordings in the inversion, because there is still some controversy about the real entity of the afterslip and post-seismic displacement they may contain, so that any modeling attempt unavoidably requires some *a-priori* assumptions [cf. *Banerjee et al.,* 2007; *Chlieh et al.,* 2007; *Hoechner et al.,* 2008].

The purpose of the present paper is two-fold. First, to infer simultaneously the main kinematics rupture parameters (slip, rake, rupture velocity); second, the estimation of the rigidity of the source zone. These estimations have been performed by means of a nonlinear inversion combining datasets of different nature. In order to have the rigidity as a free parameter in the inversion, we combined a slip-based model for the tsunami generation with a

moment-based model for the coseismic displacement at the far-field GPS stations. We thus exploited the proportionality between the slip and the seismic moment, through the rigidity (and area) of the source zone.

As pointed out in a series of papers [*Bilek and Lay,* 1998; *Bilek and Lay,* 1999; *Geist and Bilek,* 2001], rigidity values along interplate megathrust faults in subduction zones can be significantly lower than Preliminary Reference Earth Model (PREM) values [*Dziewonski and Anderson*, 1981]. This has the net effect of increasing the slip corresponding to a given seismic moment – because of the proportionality between the moment and the slip through rigidity (and fault area) – and consequently to increase the coseismic displacement and the initial tsunami amplitude. The above estimates are based on the proportionality existing between rigidity itself and source duration, when assuming constant stress drop [*Bilek and Lay,* 1999]. In particular, depth-dependent variations of the rigidity are suggested by the analysis of both 2004 Sumatran earthquake aftershocks and of earthquakes occurred before 2004, which feature longer durations for shallower events [*Bilek*, 2007].

Here, we independently determined rupture velocity and rigidity for different portions of the source zone. We also investigated along-strike variations of the fault-zone character. There is in fact strong evidence of a unilateral rupture propagating from South to North, but propagating slower in the northern part [e.g. *Ammon et al.*, 2005; *Menke et al., 2006*]. This is perhaps due either to a change in the frictional conditions and/or source zone rigidity, or resulting from structural variations of the subduction zone [*Kennett and Cummins,* 2005; *Shapiro et al.,* 2008].

In what follows, we first describe the data selection and pre-processing, along with the Green's functions generation strategy relative to each of the datasets. Then, we discuss the adopted source geometry parameterization. Later, synthetic checkerboard tests are used to

assess the resolving power, both for separate and joint inversions. Finally, the results obtained for the Sumatra earthquake and tsunami are shown and discussed.

2. Data and modeling

Tsunami (tide-gage and satellite altimetry) data selection and processing

After a careful inspection of the available tide-gage records in the Indian Ocean, we selected 13 stations (Fig. 1, and Tab. 1), which is more or less the same dataset used in previous tide-gage inversions [*Tanioka et al.,* 2006b; *Piatanesi and Lorito,* 2007; *Fujii and Satake*, 2007]. The criteria for selection have been a good signal to noise ratio, as well as a sufficient azimuthal distribution around the earthquake source.

Some of the records were available as plots made by analogic devices [HDRTN]. We digitized them with a sampling interval of 5 minutes. The digitized marigrams as well as the Sibolga marigram [GGCI] included ocean tides that we removed by high-pass filtering the records. All other marigrams were recorded by digital instruments [GLOSS/UHSLC; NIO], with sampling intervals ranging from 2 to 10 minutes. They were available on the web as de-tided residuals, and then they are directly comparable to our simulated marigrams that do not include tidal effects. We chose for each of the selected records a time window that includes, in most of the cases, only the first few oscillations after the first tsunami wave arrival. We thus try to minimize the contribution to signals of local effects (e.g. resonance of the bays, reflections), which could shadow information about the seismic source and are more difficult to simulate, due to eventual inaccuracy of the bathymetric model.

The tsunami wave was also recorded at open sea – in the middle of the Indian Ocean – by radar altimeters on board of the Jason-1, Topex/Poseidon, Envisat and GFO satellites [*Gower*,

2005; *Smith et al.*, 2005]. We have downloaded the datasets recorded by two of them from the web archive of the Jet Propulsion Laboratory [PO.DAAC]. We chose to employ only Jason-1 and Topex altimetry records, as they captured the leading tsunami wave while it was propagating westward, roughly 2 hours after the earthquake. Other altimeter satellites recorded the tsunami later on, thus having a poorer signal to noise ratio and including secondary waves reflected by the Indian coasts.

The satellites cyclically cover the same tracks, that is the same orbits with respect to the Earth's surface, and each of those is termed a "pass". The portions of Jason-1 and Topex pass 129 we considered in this study are shown in Fig. 1. We chose such portions with attempting to include as much as possible the main wave and minimizing the presence of recording gaps [cf. *Ablain et al.*, 2006]. Jason-1 recorded the tsunami signal for about 11 minutes during its pass 129 (cycle 109). Topex recorded the tsunami wave on pass 129 (cycle 452). We first averaged a few cycles preceding the tsunami, and then subtracted the result from the signal in order to extract the tsunami signal from the background [cf. *Fujii and Satake*, 2007].

Tsunami forward modeling, bathymetry, and Green's functions

Tsunamis are considered long shallow-water gravity waves, since their wavelength is usually much larger than the sea depth. In this study we used the nonlinear shallow water equations written as follows

$$\begin{cases} \dfrac{\partial(z+h)}{\partial t} + \nabla \cdot [\mathbf{v}(z+h)] = 0 \\ \dfrac{\partial \mathbf{v}}{\partial t} + (\mathbf{v} \cdot \nabla)\mathbf{v} = -g\nabla z + \mathbf{C} \end{cases} \qquad (1)$$

In eqs. (1), z represents the water elevation above sea level, h the water depth in a still ocean, $\mathbf{v}$ the depth-averaged horizontal velocity vector, g the gravity acceleration, and $\mathbf{C}$ the Coriolis force. The boundary conditions are pure wave reflection at the solid boundary (coastlines) and

full wave transmission at the open boundary (open sea). The equations are solved numerically by means of a finite difference technique on a staggered grid [*Mader*, 2001]. The initial seawater elevation is assumed to be equal to the coseismic vertical displacement of the sea bottom, computed through the Okada's analytical formulas [*Okada*, 1992], while the initial velocity field is assumed to be identically zero. Numerical modeling of the tsunami is carried out in the domain depicted in Fig. 1 with 1 arc-minute of spatial resolution for the simulation of the tide-gage records and 2 arc-minutes for the simulation of the satellite recordings, with consequently adjusted time step to ensure numerical stability.

As a bathymetric dataset for the generation of the tsunami Green's functions, we employed the GEBCO dataset [2003, and updates http://www.bodc.ac.uk/data/online_delivery/gebco/ (last accessed March 2009)]. This dataset is mainly based on ship soundings data; however, the location and density of the ship tracks are not explicitly stated in the GEBCO documentation [*Marks and Smith*, 2006]. We therefore decided to follow the practice broadly used in some recent papers [*Fujii and Satake*, 2007; *Geist et al.*, 2007; *Grilli et al.*, 2007; *Hébert et al.*, 2007; *Iouaualen et al.*, 2007; *Sindhu et al.*, 2007; *Lorito et al.*, 2008b; *Fujii and Satake*, 2008], whose authors merged different bathymetric datasets. We then scanned and geo-referenced 33 nautical charts (Fig. 1, Tab. 2) that we subsequently digitized, for a total of 1.945.328 data points. We paid special attention to include shallow water regions both around the tide-gage locations and in the source zone. The digitized bathymetric dataset is available upon request to S.L. (stefano.lorito@ingv.it). Before merging the digitized and GEBCO bathymetries, we removed all the points with elevation z in the range -200 m < z < 10 m from the regions of GEBCO covered by the points digitized from the nautical charts. This step allowed to replace the most inaccurate points in GEBCO and to reconstruct the coastlines basing on the digitized dataset. At this point we merged the datasets and interpolated them on a regular grid of 0.5 arc-min spacing. We used an interpolation code (developed by Pavel

Sakov, and available at http://geog-pc40.ulb.ac.be/grass/nnbathy/) that implements the natural neighbours algorithm [*Sambridge et al.*, 1995]. We then downsampled the gridded bathymetry to 1 arc-min with the "blockmean" GMT command, and finally smoothed the dataset by means of the GMT "surface" command, with a tension of 0.35 [*Smith and Wessel*, 1990].

The usual way to deal with the problem of retrieving the slip distribution on the fault from tsunami data is to first subdivide the fault plane into subfaults and then compute the Green's functions – i.e. the tsunami waveform at a station produced by each of the subfaults – by solving the linear form of eqs. (1). The tsunami waveforms produced by the whole source are then calculated as a linear combination of the Green's functions. The linear approximation is no longer valid for tsunami propagation in very shallow water and when the wave amplitude is relatively large. We faced this issue by following the approach of *Piatanesi and Lorito* [2007]. We used the nonlinear shallow-water equations to compute the Green's functions matrices $\mathbf{H}_{GAGE,sf}$ and $\mathbf{H}_{SAT,sf}$, corresponding to tide-gage and satellite datasets respectively (label sf indicates a generic subfault). We used "unit" slip amplitude $d_0 = 10m$ for each elementary subfault, since this is roughly the mean slip value along the whole fault, according to seismic moment estimations [*Stein and Okal*, 2005]. We repeated the calculations two times for each subfault, with mutually orthogonal rake angles of $\pi/4$ and $3/4\pi$. We exploited the linear approximation only when performing the linear combination of the Green's functions of the single subfaults (roughly speaking, we linearized the problem around the mean slip value). Given any slip and rake distribution d_{sf}, r_{sf}, where the subscript sf ranges within the entire set of subfaults, the synthetic waveforms then read:

$$\begin{cases} \mathbf{H}_{GAGE}(\mathbf{X},t) = \sum_{sf} \frac{d_{sf}}{d_0} \left[\cos(r_{sf} - \pi/4) \mathbf{H}^{\pi/4}_{GAGE,sf}(\mathbf{X}, t + \delta t_{sf}) + \sin(r_{sf} - \pi/4) \mathbf{H}^{3/4\pi}_{GAGE,sf}(\mathbf{X}, t + \delta t_{sf}) \right] \\ \mathbf{H}_{SAT}(\mathbf{X},t) = \sum_{sf} \frac{d_{sf}}{d_0} \left[\cos(r_{sf} - \pi/4) \mathbf{H}^{\pi/4}_{SAT,sf}(\mathbf{X}, t + \delta t_{sf}) + \sin(r_{sf} - \pi/4) \mathbf{H}^{3/4\pi}_{SAT,sf}(\mathbf{X}, t + \delta t_{sf}) \right] \end{cases} \quad (2)$$

where the labels $\pi/4$ and $3/4\pi$ distinguish between orthogonal rake angles, for each of the subfaults. The rupture is moreover allowed to propagate at a velocity v_{sf} from the South to the North, reflected by the delay δt_{sf} from the earthquake origin time.

In detail, we obtained the Green's functions $\mathbf{H}_{GAGE,sf}$ at the tide-gage stations by sampling the simulated water height evolution in correspondence of the actual tide-gages coordinates and with the actual sampling rate (Tab .1). We conversely obtained the satellite Green's function $\mathbf{H}_{SAT,sf}$ for each point of the satellite track by spatially averaging the water height in square regions of 4 arc-minutes, as this roughly corresponds to what the satellite altimeter actually measure [cf. *Gower*, 2005]. We moreover took into account that the altimetry recording is a function of both space and time, as the satellites measure at different times along their tracks [cf. *Sladen and Hébert*, 2008].

Geodetic forward modeling and GPS dataset

Static surface deformation field data associated with the 2004 Sumatra earthquake shows that the elastic deformation of Earth caused static offsets recorded at continuously operating GPS stations at distances of up to 4500 kilometers off from the epicenter [*Boschi et al.*, 2006; *Banerjee et al.*, 2007].

We modeled the associated coseismic surface displacements adopting the theoretical model of global coseismic deformation originally proposed by *Piersanti et al.* [1995], and later refined by *Soldati et al.* [1998] and by *Boschi et al.* [2000]. It is a semi-analytical, spherical model which assumes an incompressible, layered, self-gravitating Earth with Maxwell linear viscoelastic rheology, and it is capable of modeling both elastic and viscoelastic responses induced by a seismic dislocation.

The set of differential equations governing the model is:

$$-\rho_0 \nabla \widetilde{\phi}_1 - \nabla(\widetilde{\mathbf{u}} \cdot \rho_0 g_0 \mathbf{e}_r) + \nabla \cdot \widetilde{\mathbf{T}} = \rho_0 \widetilde{\mathbf{f}} \tag{3}$$

$$\nabla \cdot \widetilde{\mathbf{u}} = 0 \tag{4}$$

$$\nabla^2 \widetilde{\phi}_1 = 0 \tag{5}$$

$$\widetilde{\mathbf{T}} = 2\mu \widetilde{\mathbf{E}} + \widetilde{p}_1 \mathbf{I} \tag{6}$$

$$\widetilde{\mathbf{E}} = \frac{1}{2}\left[\nabla \widetilde{\mathbf{u}} + (\nabla \widetilde{\mathbf{u}})^T\right] \tag{7}$$

where the tilde denotes the Laplace-transformed variables and the subscripts *0* and *1* refer to the equilibrium and perturbed values, respectively; g_0 is the reference gravity acceleration, p_1 is the incremental pressure, ρ_0 is the density, $\mathbf{u}$ is the deformation; ϕ_1 is the perturbation to geopotential and $\widetilde{\mu}$ is a Laplace-trasformed rigidity defined as $\widetilde{\mu} = \frac{\mu s}{s + \mu/\eta}$, where s is the Laplace complex variable, μ the rigidity and η the viscosity. Eq. (3) states the momentum conservation in the presence of a seismic dislocation represented by the equivalent body force $\widetilde{\mathbf{f}}$. Eq. (4) is the incompressibility condition and eq. (5) is the Laplace equation for the perturbation to gravitational potential $\widetilde{\phi}_1$ due to the displacement field $\widetilde{\mathbf{u}}$. Eq. (6) relates the incremental stress field $\widetilde{\mathbf{T}}$ to the infinitesimal strain tensor $\widetilde{\mathbf{E}}$ via the viscoelastic constitutive relation. We refer the reader to works cited above for details concerning both the analytical solution of the eqs. (3-7) and the associated numerical issues.

We calculated the coseismic GPS offsets induced by the Sumatra earthquake at a station subset of the 108 far-fields GPS static offsets assembled by *Banerjee et al.* [2007] (their tables S1 and S2 in the electronic supplement). In particular, we selected 84 GPS stations with longitudes between 65° E and 130° E and latitudes between 25° S and 45° N (Tab. 3, some in Fig. 1) since the incompressibility approximation may lead to an overestimation of displacements in the very far-field [*Boschi et al.*, 2006; *Banerjee et al.*, 2005]. The selected

data include the coseismic horizontal displacement vectors derived from the analysis of continuous GPS (CGPS) measurements by *Banerjee et al.* [2007] plus the CGPS and campaign GPS (SGPS) coseismic horizontal displacements derived from *Vigny et al.* [2005], and corrected for postseismic relaxation by *Banerjee et al.* [2007]. The 84 far-field stations are both CGPS sites of permanent global and regional GPS networks (principally from IGS [*Dow et al.*, 2005] and SuGAr) and SGPS sites from surveys conducted by regional institutes (for further details, see *Banerjee et al.* [2007] and references therein).

In the joint inversion we excluded the northern Sumatra and the Andaman and Nicobar Islands SGPS coseismic horizontal surface displacements provided by *Banerjee et al.* [2007] (their tables S3 and S4 in the electronic supplement) because there are some (partly) controversial findings by different authors, regarding the amount of afterslip and/or post-seismic signal that may be superposed to the coseismic contribution in such measurements [cf. *Banerjee et al.*, 2007; *Chlieh et al.*, 2007; *Hoechner et al.*, 2008]. As we will discuss later, the exclusion of near-field data comes at the price of a resolution loss on small-scale source structure.

We employed a four-layer stratification model, which includes an 80 km elastic lithosphere, a 200 km thick asthenosphere, a uniform mantle, and a fluid core. All the mechanical parameters have been obtained by means of a weighted volume average of the corresponding parameters of the PREM [*Dziewonski and Anderson*, 1981].

Each subfault plane is subdivided into a two-dimensional distribution of point seismic sources, located on the nodes of a grid with 15 km spacing. A unit seismic moment $M_0 = \mu_0 A_0 d_0$ is fixed for each elementary subfault, where $\mu_0 = 56\ GPa$ is a "unit" subfault rigidity, A is the subfault area and $d_0 = 10m$ is a "unit" slip, which is the same value we used for the tsunami Green's functions. At the GPS stations coordinates $\mathbf{X}$, the total coseismic

displacement $\mathbf{U}_{GPS,sf}$ due to each subfault – the Green's function – is computed by linear superposition of the displacements $\mathbf{u}^i_{GPS}$ due to N_{sf} equally spaced point sources, i.e.

$$\mathbf{U}_{GPS,sf}(\mathbf{X}) = \sum_{i=1}^{N_{sf}} \mathbf{u}^i_{GPS}(\mathbf{X}) \qquad (8)$$

For each of the subfaults, the calculation is performed for each of the mutually orthogonal rake angles $\pi/4$ and $3/4\pi$. Given any slip, rake and rigidity distribution d_{sf}, r_{sf}, μ_{sf} over the entire source, the synthetic displacement at the GPS stations is then calculated as a combination of the contribution by the single subfaults Green's functions, and of mutually orthogonal rake pairs for each of the subfaults:

$$\mathbf{U}_{GPS}(\mathbf{X}) = \sum_{sf} \frac{\mu_{sf} d_{sf}}{\mu_0 d_0} \left[\cos(r_{sf} - \pi/4)\mathbf{U}^{\pi/4}_{GPS,sf}(\mathbf{X}) + \sin(r_{sf} - \pi/4)\mathbf{U}^{3/4\pi}_{GPS,sf}(\mathbf{X}) \right] \qquad (9)$$

or, equivalently,

$$\mathbf{U}_{GPS}(\mathbf{X}) = \sum_{sf} \frac{M_{sf}}{M_0} \left[\cos(r_{sf} - \pi/4)\mathbf{U}^{\pi/4}_{GPS,sf}(\mathbf{X}) + \sin(r_{sf} - \pi/4)\mathbf{U}^{3/4\pi}_{GPS,sf}(\mathbf{X}) \right] \qquad (10)$$

where $M_{sf} = \mu_{sf} A_{sf} d_{sf}$ is the seismic moment of the subfault with area equal to A_{sf}.

3. Parameterization

Fault geometry, subfaults

As a source zone model for the Sunda megathrust we used the structural representation proposed by *Subarya et al.* [2006], their "model B". This is a model based on teleseismic and local earthquakes observation as well as on volcanoes location. It is a curved plate interface, which dips at only a few degrees at the trench, and projects to about 100 km depth beneath the volcanic arc. The fault model features an increasing dip in the northern profiles. We averaged

the nodes of *Subarya et al.* [2006] into much broader rectangular fault patches (Table 4, Fig. 1). We thus defined a set of 18 subfaults, with variable strike, dip, area, position, and depth. We ended up with two rows of 9 subfaults each, one shallower and one deeper, extending from about 1.5°N to 14°N, that is from Simeulue Island to the Andaman Islands. The total linear length spanned by the entire fault is almost 1500 km, with a subfault length of ~160 km and a width of ~105 km on the average. The subfaults in the shallower row extend in depth from about the surface down to ~10 km; those in the deeper row from ~10km to ~36km.

Inversion parameters

We have subdivided the fault plane into subfaults and used the Green's functions method.

In the case of the tsunami Green's functions, slip and rake (d_{sf}, r_{sf}), are the input parameters for the Okada's formula. The initial vertical displacement transferred to the water is then propagated to both the tide-gages and along satellite tracks by numerical solution of nonlinear shallow water equations. Additionally, we included a rupture velocity v_{sf}, representing the (variable) velocity of the rupture while propagating from South to North. We only imposed that the rupture be unilateral. Conversely, the 4 southernmost subfaults, around the epicenter and comprising Simeulue islands (Fig. 2), rupture simultaneously. We moreover allowed the shallow and deep subfaults subsets to rupture independently, so that the rupture may propagate at different velocities in the shallower and in the deeper part of the source.

The GPS Green's functions are calculated with the seismic moment $M_{sf} = \mu_{sf} A_{sf} d_{sf}$ (and rake r_{sf}) as input for a global coseismic deformation model, yielding the horizontal displacement at the far-field GPS sites.

To summarize, the synthetic marigrams and the synthetic offset at GPS stations can be represented as:

$$\begin{cases} \mathbf{H}_{GAGE}(\mathbf{X},t) = \sum_{sf} d_{sf} \tilde{\mathbf{H}}_{GAGE,sf}(\mathbf{X}, r_{sf}, v_{sf}) \\ \mathbf{H}_{SAT}(\mathbf{X},t) = \sum_{sf} d_{sf} \tilde{\mathbf{H}}_{SAT,sf}(\mathbf{X}, r_{sf}, v_{sf}) \end{cases} \quad (11)$$

$$\mathbf{U}_{GPS}(\mathbf{X}) = \sum_{sf} \mu_{sf} d_{sf} \tilde{\mathbf{U}}_{GPS,sf}(\mathbf{X}, r_{sf}) \quad (12)$$

where the tilde appears as we incorporated into the Green's functions all parameters but slip and rigidity of the single subfaults.

An inversion of the tsunami data alone would allow to retrieve slip, rake, and rupture velocity, by means of eqs. (11); an inversion of the GPS data alone would allow to retrieve seismic moment and rake, by means of eq. (12), and indirectly the slip for a given rigidity value. The joint inversion of the tsunami and GPS datasets allows to invert four free parameters: slip, rake, rupture velocity, and rigidity. Additionally, eqs. (11) are non-linear in the velocity, as well as eq. (12) is non-linear because of the product between rigidity and slip: a simultaneous inversion of the whole parameter set therefore requires a non-linear inversion method.

With the use of a single modeling tool for coseismic displacement modeling (for both GPS and tsunami) the rigidity inversion would not have been possible. We thus chose a slip-based model to compute the vertical displacement in the near-field, and a moment-based model to calculate the horizontal displacement in the far-field. This approach has the advantage of letting only the slip as a coefficient in eqs. (11), then allowing the rigidity to be determined by means of eq. (12).

In what follows, we discuss our choices. The Okada's formulas, that is the elastic homogeneous half-space approximation, is widely used for the calculation of the near-field displacement [e.g., *Fujii and Satake*, 2007; *Pietrzak et al.*, 2007]. While sphericity may be ignored at the fault scale, crustal layering, or the presence of a superficial soft sediment layer, could play a significant role. In the present case of a low-angle thrust fault, however, the differences between the vertical displacement generated using Okada's formulas and using a

layered model such as EDGRN/EDCMP [*Wang et al., 2003*] are not in fact really pronounced, say less than 10% [*Geist,* 1999; *Amoruso and Crescentini,* 2004; *Zhao et al.*, 2004; *Megna et al.*, 2008]. Additionally, slip-based source models are only slightly dependent on rigidity, if not at all [*Tinti and Tonini*, 2005; *Geist et al.,* 2007]. On the other hand, it is not uncommon to combine different modeling tools or geometries, depending on the nature of the data. An example is the combined inversion of seismic, tsunami and geodetic data of *Ichinose et al.* [2007]. They compute the vertical coseismic displacement Green's functions using a layered Earth's model, while the tsunami Green's functions are computed using the equations of Okada to derive the initial sea surface height changes. Our scheme is moreover comparable to that adopted by *Rhie et al.* [2007], who calculate the GPS offsets in the near-field with a flat layered model, and the long period Green's seismic waveforms by means of a normal mode summation method in spherical geometry with a PREM-layered rheology. Their formulas at page 2 are indeed the equivalent of our eqs. (11) and (12). The most remarkable difference is that they *a-priori* fix the fault rigidity.

4. Nonlinear inversion

Inversion technique

We simultaneously inverted for slip, rake, rupture front velocity, and fault rigidity. We then faced a nonlinear inversion problem and solved it following *Piatanesi and Lorito* [2007], and *Piatanesi et al.* [2007], which use the "heat bath algorithm" implementation of the simulated annealing technique [*Rothman*, 1986]. This technique is based on a large sampling of the model space, and progressive concentration of the search on regions characterized by low values of the cost function, i.e. where the optimal models are likely to be found.

We compared the observed and synthetic datasets by means of two different cost functions for the tsunami and geodetic datasets. For the tsunami dataset, which is composed of time series, we used a cost function that has proven to be sensible both to amplitude and phase matching [*Spudich and Miller*, 1990; *Sen and Stoffa*, 1991]. It is expressed as follows:

$$E(m) = \sum_{k=1}^{N} \left[1 - \frac{2\sum_{t_i}^{t_f} (u_O(t) u_S(t))}{\sum_{t_i}^{t_f} u_O^2(t) + \sum_{t_i}^{t_f} u_S^2(t)} \right]_k \qquad (13)$$

In eq. (2) u_O and u_S are the observed and synthetic waveforms respectively, t_i and t_f are the lower and upper bounds of the time window and N is the number of records used in the inversion. At each inversion step, the above cost function (13) is evaluated two times, one for the tide-gage misfit, and one for the satellite data misfit. We assigned a relative weight to each tide-gage contributing to the cost function in order to take into account non-uniformity in the sampling rate of the records (see Table 1). We also assigned a relative weight of one fourth to Topex data with respect to Jason-1 data, to take into account the disproportion between their latitude coverage (Fig. 1). On the other hand, for the geodetic dataset, we used a standard L_2-norm as a cost function to quantify the misfit between experimental and synthetic datasets.

In the implementation of the joint inversion, the cost functions for the three datasets are summed up to obtain the global cost function. Relative weights are assigned to each cost function, in order to guarantee the maximum possible overlapping among their ranges of variation during the whole inversion. This is not straightforward, as the three separate cost functions have very different behaviors depending on their sensitivity to the variations of each parameter. We verified that a progressive increasing of the relative weight assigned to the tsunami dataset with respect to the geodetic dataset results in a progressive loss of resolution for the rigidity parameter, because the latter doesn't appear in eq. (11). On the other hand, the result of increasing the relative weight of the geodetic dataset implies a loss of resolution on

both slip and rigidity, as a consequence of the intrinsic trade off between them (eq. (12)). We then empirically tried to give, on the average, similar weights to the three datasets, by means of synthetics checkerboard tests similar to those presented in a later section. We nevertheless verified that in the "real case" inversion, the results presented below in the case of the Sumatra 2004 earthquake are quite robust with respect to weights variations around the chosen values.

We introduce *a-priori* information in the solution by imposing lower and upper bounds to the range of variation of the source parameters, and on their steps between extreme values. The slip value is allowed to vary between 0 and 35 meters on each subfault, at 1 meter steps. The rake is allowed to range between 90° and 135°, at 5° steps. The rupture velocity between 0.25 and 5.0 km/s, at 0.25 km/s steps. Finally, the rigidity is allowed ranging between 5 and 50 GPa, at steps of 5 GPa.

Inversion of tsunami data: checkerboard test

As a first stage, we studied the resolution of the tsunami data, both recorded by satellites and tide-gages. To check the effectiveness of our method in inverting for both the slip and rake distribution and the rupture velocity, we performed a series of synthetic tests [cf. *Piatanesi and Lorito*, 2007; *Lorito et al.*, 2008a; *Lorito et al.*, 2008b].

Figure 2 (left panel) depicts the synthetic rupture model we used in the main synthetic test. It consists of a slip distribution having a checkerboard pattern, with slip values alternating between 5 and 15 meters on adjacent subfaults. We assigned three different values to the rake, letting its value change only along strike. We chose a rake of 90° for the group of the 6 southernmost subfaults (both shallow and deep), then 130° for the next 6, and again 90° for the 6 northernmost ones. We verified by means of some preliminary tests (not shown) that allowing three different values along strike is a good compromise between the resolving

power of our dataset and the possibility of following the rake variation along strike for the 2004 earthquake [cf. *Menke et al.*, 2006]. During the inversion, we have consequently forced the rake values within each of the 6-subfaults groups to be equal, as in the target synthetic model. The rupture in this test is chosen unilateral from South to North, as in the Sumatra earthquake. The target model features four different rupture front velocities. The rupture front is fixed to propagate with different velocities in the shallower and the deeper subfaults, and for both of them it slows down in the second half of the rupture. Along the shallower ones, the rupture is imposed to propagate at an average velocity of 1.5 km/s from the epicenter to about 6°N, and then at 1 km/s. Along the deeper subfaults, the velocity is fixed to 2.5 km/s south of 6°N and to 2 km/s north of 6°N. Again, during the inversion, the explored models are forced to have the same velocity pattern. Similarly to what we have done for the rake, we have proven with other synthetic tests (not shown) that this is the spatial resolution limit for the inversion of the rupture front velocity.

The synthetic waveforms, produced with such a source process both for tide-gages and satellites, are corrupted by adding a gaussian random noise with a variance that is 10% of the clean waveform amplitude variance [cf. *Sen and Stoffa*, 1991; *Ji et al.*, 2002], to mimic eventually non-modeled uncertainties.

The results indicate that the source process is in principle very well constrained by the tsunami data, provided a careful tuning of the spatial resolution for each of the parameters. The best inverted model is in fact very similar to the target one: the checkerboard shape of the slip distribution is very well reproduced (right panel of Fig. 2, column 2 of Tab. 5), and the slip values have a maximum difference to the target ones of 1 meter. The rake distribution is estimated exactly (Tab. 5, col. 3). The rupture velocity distribution also is estimated exactly (see Table 5, col. 2), with the exception of the deeper northernmost stretch of the source, where the difference between the inverted and the target velocity is however only 0.25 km/s.

Inversion of geodetic data: checkerboard test

As a second stage, we repeated the checkerboard test with the geodetic dataset. In this case, the free parameters to be determined by means of the inversion are the slip and the rake distributions. We thus didn't allow the rigidity value to vary during the inversion, which is possible only in the joint inversion of tsunami and geodetic data. The target model (Fig. 3, left panel) we used to generate a synthetic dataset of horizontal displacements at the GPS stations is the same as in the checkerboard test with the tsunami data (Fig. 2, left panel). Of course, the static GPS measurements are insensitive to the rupture velocity. We corrupted both North and East components of each synthetic GPS data point by adding a normally distributed random value, with a variance equal to the square of the error on the real data.

The checkerboard test in the case of the geodetic data has given a negative result (right panel Fig. 3 and Tab. 5, cols. 3-4). Despite of the almost perfect agreement between the synthetic and the inverted GPS vectors, the checkerboard pattern of the slip distribution is totally missed. Only the rake distribution is quite well recovered, with exception of the northernmost stretch, where the difference between target and inverted values is 20°. We repeated the test even with a clean dataset, i.e. without noise added to the synthetic data, and obtained comparably loose results. On one side this supports the choice of inverting the rake on a broader spatial scale than that of the single subfaults, as already done for the tsunami data. On the other side though, because the cost function of the inverted model has a relatively low value (i.e. the synthetic and the inverted horizontal displacements are very similar), it is likely that the problem is ill conditioned and the solution is not unique. In other words, given the present geodetic data distribution, it is impossible to constrain the slip distribution at the scale of the single subfault.

We then repeated the checkerboard test with bigger patches of slip in the target model (Figure 4, left panel). This time we divided the fault into 3 broader groups of subfaults, having the same spatial scale of the rake distribution. So we imparted 5 meters of slip and a rake of 90° to the southernmost patch, 15 meters and 130° to the intermediate, 5 meters and 90° to the northernmost. We added noise as before to the synthetic dataset.

In this case we have been able to recover the target pattern fairly well, both in terms of slip and rake, as can be seen in figure 4 (and Table 5, cols. 6-7). This confirms that the geodetic dataset has a lower spatial resolution than the tsunami dataset, as far as the slip distribution is concerned. Additionally, we noticed that the inversion performed better in the southernmost and middle part of the source, whilst both inverted slip and rake values are in comparison farther from the target values in the northernmost stretch of the source. The geodetic data then constrain the source process particularly well south of about 9°N.

The above results are consistent with the features of our geodetic dataset, in which the near-field stations have not been included for the reasons discussed above, so that it cannot be sensitive to detailed small-scale source structure [cf. Chlieh et al., 2007]. Nevertheless, the far-field geodetic dataset can contribute to the inference of the seismic moment on a broader scale, and consequently, in the joint inversion with the tsunami data, to the rigidity inference on the same scale.

Joint inversion of tsunami and geodetic data: checkerboard test

The last checkerboard test we performed is a joint inversion of the whole dataset of this study, i.e. the tide-gages, the satellites and the geodetic data.

The setup of the target source (Figure 5, left panel) is the same as in the case of the tsunami dataset. We moreover assigned two different rigidity values, 30 GPa to the group of the 8 southernmost subfaults, and 10 GPa to the group of the remainder 10 subfaults, which are

those north of about 6°N (gray ellipses of Figure 5, left panel). Similarly to what we have done before, we verified with some preliminary checkerboard tests (not shown), performed on synthetic sources with rigidity varying at a finer scale, that two rigidity values on quite broad zones is in this case very close to our resolution limit.

The results of the checkerboard test are satisfactory in the case of the joint inversion (right panel in Fig. 5 and Tab. 5, cols.8-9). The tsunami and geodetic datasets combined are then in principle able to constrain both the source process and the source zone rigidity (even if on a broader scale). In particular, the test demonstrated that we have got rid of the intrinsic trade off between slip and rigidity implied by eq. (12), likely because the slip distribution is well constrained by the tsunami dataset. The checkerboard pattern of the slip distribution is in fact very well reproduced, and the slip values have a maximum difference to the target ones of 2 meters. The rake values are exactly recovered almost everywhere, with exception of the central part, where there is a slight difference (5°) between target and inverted values. The rupture velocity distribution is exactly estimated, as well as the rigidity values.

Joint inversion of tsunami and geodetic data: the Sumatra 2004 earthquake

We used the setup of the checkerboard test described in the previous section to retrieve the source process of the December 2004 Sumatra earthquake, by means of a joint inversion of the tsunami and geodetic datasets.

Timing corrections of the Green's functions for Ranong, Krabi, Trang, Tarutao, Visakapatnam, Paradip, and Tuticorin were made, because we observed at these stations systematic differences between recorded and simulated phases. Relatively low resolution and uncertain nearshore bathymetry could have lead to inaccurate calculated travel times. In the present case, however, we verified that the positions of the slip patches, as well as the inverted rupture velocity, are only slightly dependent on the travel time adjustments.

The best model results are shown in Figure 6, left panel. The numerical values of each of the inverted parameters are listed in Table 6, columns 1 and 2.

The best source model we estimated for the 2004 earthquake features the maximum slip concentration in a broad patch around the epicenter and South of 6°N. In this zone there are 4 subfaults with slip values greater than 20 meters, and with a peak value of 34 meters. The rake in this patch is 95°. Further to this southernmost and biggest patch of slip, there are two northernmost smaller slip patches. The first one is centered at about 8°N with slip ranging from 12 to 18 meters and a rake of 95°. A third slip concentration is seen at depth – 10 to 36 km – below the Andaman islands (11 to 14°N), with slip between 6 and 8 meters, and rake 135°.

Our model features a rupture that propagates at a velocity that is 3.25 km/sec in the deeper southernmost segment (up to about 6°N), before slowing down to 2 km/sec in the northernmost and deeper part of the source. This corresponds to a total rupture duration of about 10 minutes. In the shallower southernmost segment the ruptures instead propagates slower from the beginning, at 2 km/s, and then much slower (0.5 km/s) in the northernmost shallower segment. This corresponds to a total rupture duration of 20 minutes, if one considers a front traveling along the shallower part and stopping at about 9-10°N. However, the rupture velocity cannot be well constrained here, for there is only one subfault slipping significantly, and then the slip goes rapidly to almost zero in the next subfault. This large uncertainty is highlighted by a question mark attached to the velocity value in Figure 6.

We estimated a rigidity value of 20 GPa for the source portion south of 6°N. This has to be considered as an average rigidity of the layer spanning from the surface down to 36 km of depth. Conversely, for the northernmost portion of the source, we estimated a rigidity value of 30 GPa. The latter has to be associated mostly to the deeper part of the source zone – 10 to 36 km – because, as already noticed, almost all the slip occurs on the deeper subfaults at North,

with the exception of only one shallow subfault. Using these values for the rigidity, the seismic moment associated to our best solution is $6.63 \cdot 10^{22}$ Nm, corresponding to a magnitude Mw=9.15.

The errors on the model parameters are estimated, following *Piatanesi and Lorito* [2007], by means of an *a-posteriori* analysis of the ensemble of the models explored during the search for the best model. We here used only a subset of the explored models, i.e. we constructed the ensemble with only those models having a cost function exceeding by 1% the minimum value reached during the inversion. We first calculated the average model for each of the parameters, and then estimated the errors as the weighted standard deviation of each parameter. We used as a weighting function the inverse of the cost function. Both the average model and the associated errors are reported in Table 6, columns 3 and 4. The average source model is reported in Figure 6, right panel. The parameter values vary smoother along the average model than they did in the best model. For example, the rake changes more "gently" from 94° to 125°, passing through 104° in the middle of the source. Also, in the average model, the slip maxima in the southern portion of the source are lower than that of the best model, and the slip value never vanishes. This model is constructed by averaging all models featuring a low cost function, then having a significant probability of being good source models. Then, the average model, along with its associated errors, may indicate that the best model is eventually "overfitting" the data, so being a measure of how much epistemic and experimental errors are mapped into the retrieved source models. This may be the case, for example, when the best and average models are very different, or when the uncertainties are very large.

The comparison between the experimental datasets, and the synthetic ones generated with the best source model, is shown in Fig. 7. The simultaneous agreement of the tsunami waveforms at the tide-gages, the waveforms recorded by satellites, and the geodetic measurements with

their synthetic counterparts is noticeable, particularly if one takes into account the intrinsic uncertainties in modeling, and the experimental dataset inhomogeneity. The comparison between the data and the predictions of the average model (Fig. 8) is only slightly worst than that found with the best model. This indicates that the fit between data and synthetics is still acceptable, in the range defined by the comparison between Fig. 7 and 8, or by the errors listed in Table 6. Such variations are then likely to give a correct idea of the uncertainties associated to our source model.

5. Discussion

We found a slip distribution featuring most of the earthquake energy released around the Northern end of Sumatra, and further releases of slip through the Nicobar Islands and up to the Andaman Islands, with an overall length of the rupture of at least 1300 km. The magnitude Mw=9.15 we retrieved is consistent with previous estimations based on data of different nature [*Stein and Okal*, 2005; *Chlieh et al.*, 2007].

The presence of, at least, the two southernmost slip patches is a persistent feature of various models, as for example that of *Fujii and Satake* [2007], obtained by means of a joint inversion of tide-gage and satellite data, or the model proposed by *Pietrzak et al.* [2007], who combine GPS and coral reefs data.

In the present case, however, the slip in the best model is nearly zero in two of the southernmost subfaults near to the epicenter (namely subfaults 1 deep and 2 shallow, Table 6), while it is larger at the same places in the average model. This emphasizes the presence of a possible epistemic source of error due to the size of the subfaults. Nevertheless our source produces maximum water elevation values consistent with the maximum measured runup,

which is around 30 meters in North-western Aceh [*Borrero*, 2005; *Tsuji et al.*, 2005; *Jaffe et al.*, 2006]. However, we do not expect to reproduce the details of the 2004 tsunami in the very near field, as we inverted for the entire source spanning about 1500 km and using far-field data [cf. *Geist et al.*, 2007]. Smaller subfaults, along with the constraints posed by near-field data such as the runup measurements in western Aceh, would help to better constrain the slip distribution for the 2004 earthquake at a finer spatial scale.

The third, deeper, and northernmost patch of slip is present in some recent models, as for example those presented by *Hoechner et al.* [2008], based on geodetic data, and *Sladen and Hébert* [2008], who pointed out that the relatively moderate tsunami observed at Andaman Islands may well be explained by the depth of the nearby patch.

The rake of the model rotates counter-clockwise as the rupture propagates northward, consistently to previous results [e.g. *Lay et al.*, 2005; *Subarya et al.*, 2006; *Banerjee et al.*, 2007], and is also consistent with the more oblique plates' convergence to the North.

Our model is characterized by a rupture that slows down in the northernmost segment of the source. The velocity of propagation of the rupture front has been decreasing, according to different investigators [*Bilham,* 2005; *Menke et al.*, 2006], while the rupture itself was proceeding northward. But we moreover inferred a slower rupture velocity for the shallower than for the deeper part of the southernmost source segment. The above corresponds to a total rupture duration of about 10 minutes. We find also an indication of a possibly slow rupture at about 8-9°N in the shallower part of the source, lasting up to about 20 minutes after the earthquake initiation. *Stein and Okal* [2005], first indicated the possibility of slow slip in the northern part of the source, and successively *Seno and Hirata* [2007] confirmed this finding, with a determination of the rupture velocity similar to what we found here. Nevertheless, others concluded that a slow slip component was not present or not necessary to explain the observations [Bilek, 2007; Chlieh et al., 2007; Fujii and Satake, 2007]. However, this feature

is not completely constrained by our inversion, due to the limited spatial extent of the corresponding slip patch.

The model rigidity values, that we here derive for the first time self-consistently in a joint inversion are lower than the PREM average values at the corresponding depths. This supports previous findings concerning the Sumatra 2004 earthquake source zone [*Bilek*, 2007], as well as other subduction zones [*Bilek and Lay,* 1998; *Bilek and Lay,* 1999]. Such results are derived by assuming constant stress drop and the rigidity being inversely proportional to the rupture duration; conversely, in the present study we didn't make *a-priori* assumptions in this respect.

Moreover, we found that, in the southernmost source segment, the rupture is slower near to the Earth's surface than it is at depth. This is likely to be a consequence of the rigidity increase with depth, for the rupture velocity is generally found to scale with shear wave velocity [*Bilek and Lay,* 1998], which by definition is proportional to the rigidity itself. In other words, the rupture should propagate faster in the deeper part of the source, and this is what we found with our inversion. However, as we couldn't resolve properly the variations of the rigidity with depth, we couldn't independently establish such a detailed correlation between these two parameters.

As about the along-strike variation of the fault properties, we observe that the rupture is slowing down and deepening in the northern part of the source. Thus the rigidity value we estimated (≤30GPa) is representative of the deeper portion of the source (10-36 km depth). This very low rigidity value, along with the relatively low velocity with respect to southernmost part of the source, is likely to be explained by the changes in the properties of the subducted slab indicated by *Kennett and Cummins* [2005], who find zones of relatively low ratios of shear velocities to bulk ratio in the northern part of the source, and by the presence of a low seismic velocity material under the Andaman Sea [*Shapiro et al.* 2008].

Nevertheless, *Bilek* [2007] found no evidence of frictional conditions changes at North, even if basing on a relatively scarce dataset of seismic events in the Northern Andaman segment. Finally, we used our source model to predict ground displacements in the near-field, where some geodetic campaign data exists [*Gahalaut et al.*, 2006; *Jade et al.*, 2005; *Subarya et al.*, 2006], that have been excluded from the inversion dataset for the reasons discussed above. We observe (Fig. 9) that our model clearly under predicts the observed displacement [*Banerjee et al.* (2007), tables S3 and S4 of the electronic supplement] along the Andaman and Nicobar Island. A slight deficit of the predicted horizontal deformation is present in the Northern part of Sumatra (between 5° and 6°N). This would support a significant presence of afterslip/postseimic deformation in the campaign measurements, as suggested by Chlieh et al. [2007]., As the tsunami data used in the inversion (tide-gage plus satellite) are likely to offer a good control on the slip distribution in the Northern part of the source, we consider this result quite robust, at least in the framework of 1D (layered Earth) modeling. However, as most of the data have been measured just over the island arc, they are likely to be sensible to the 3D structure of the subduction zone [*Masterlark and Hughes*, 2008], and a more sophisticated model would be necessary to settle the question.

6. Conclusions

We presented a joint inversion of tide-gage, satellite altimetry, and far-field GPS data, conducted to infer the source process and the source zone rigidity of the December 2004 Sumatra-Andaman earthquake. We inverted four free parameters: slip, rake, rupture velocity, and source rigidity.

We first performed a series of synthetic checkerboard tests. We found that the tsunami data are able to constrain the slip distribution at the spatial scale of the single subfault, whilst the far-field geodetic data may constrain the slip distribution only on a broader scale. The rake, velocity and rigidity are all constrained by the present dataset on a broader scale than the slip.

The joint inversion of the three datasets in the case of the Sumatran 2004 earthquake has confirmed results of previous inversions, with a rupture characterized by three main slip patches, among which the broadest is around the epicenter and with slip peaking at ~30 meters.

In addition to previously published papers, we found that the rupture propagated slower in the shallower than in the deeper part of the source, consistently with the fact that the rigidity should increase with depth. The rupture propagated slower also while releasing the two northernmost slip patches, where progressively less rigid material is likely to exist. The rake rotated counter-clockwise at North, according to the relative direction of the plates' convergence.

We also determined self-consistently the average rigidity of the source zone on a broad scale, which resulted significantly lower than the PREM values at the corresponding depths. The estimation of the source zone rigidity is important since it may play a significant role in the tsunami generation and, particularly for slow earthquakes, a low rigidity value is sometimes necessary to explain how a relatively low seismic moment earthquake may generate significant tsunamis [*Geist and Bilek,* 2001]. In the case of the Sumatran earthquake source, a lower-than-the-average rigidity could also be the key to explain why inversions that rely on slip-based source models [*Fujii and Satake*, 2007; *Piatanesi and Lorito*, 2007; *Pietrzak et al.*, 2007; *Hoechner et al.*, 2008; *Sladen and Hébert*, 2008] give generally greater maximum slip values (~30 meters, as in the present study) than those using moment-based models [*Ammon et al.*, 2005; *Chlieh et al.*, 2007; *Rhie et al.*, 2007]. The latter generally impose PREM like-

values to deduce the slip through the rigidity. Conversely, both kind of methods give comparable moment and consequently magnitude estimates.

As a side effect of our investigation, we found that near-field (campaign) GPS data are likely to contain first order non-coseismic signals. This prevented us from including such data into the inversion, and unfortunately posed an upper bound to the resolution on the inference of the rigidity distribution. For the same reason, we could not establish a direct correlation between rupture velocity and source rigidity at a finer scale. In the future, e.g. when and where reliable near-field geodetic data will be available after a large subduction zone earthquake, it will be possible to apply – and further validate – the approach we proposed here. This will be more robust if including a 3D modeling better representing the real structural complexity of a subduction zone.

Nevertheless, the general consistence between our source model with previous studies supports the validity of the method we proposed for the rigidity estimation from the joint inversion of geodetic and tsunami data, and will hopefully stimulate further research.

Acknowledgments

We gratefully acknowledge the contribution of A. Mautone at SISMOS/INGV, who scanned the nautical charts. Comments and suggestions by two anonymous reviewers have greatly improved this manuscript.

Some figures have been produced with Generic Mapping Tools software (Wessel and Smith, 1998). Natural Neighbours interpolation software was provided by Pavel Sakov and is available at URL: http://geog-pc40.ulb.ac.be/grass/nnbathy/ (last accessed March 2009).

References

Ablain, M., J. Dorandeu, P.-Y. Le Traon, and A. Sladen (2006), High resolution altimetry reveals new characteristics of the December 2004 Indian Ocean tsunami, *Geophys. Res. Lett.*, *33*, L21602, doi:10.1029/2006GL027533.

Ammon, C. J., C. Ji, H.K. Thio, D. Robinson, S. Ni, V. Hjorleifsdottir, H. Kanamori, T. Lay, S. Das, D. Helmberger, G. Ichinose, J. Polet and D. Wald (2005), Rupture process of the 2004 Sumatra-Andaman earthquake, *Science*, *308*, 1133-1139, doi:10.1126/science.1112260.

Amoruso, A, L. Crescentini, and C. Fidani (2004), Effects of crustal layering on source parameter inversion from coseismic geodetic data, *Geophys. J. Int., 159*, 353-364, doi:10.1111/j.1365-246X.2004.02389.x.

Banerjee, P., F.F. Pollitz and R. Bürgmann (2005), The size and duration of the Sumatra-Andaman earthquake from far-field static offsets, *Science*, *308*, 1769-1772, doi:10.1126/science.1113746.

Banerjee P., F.F. Pollitz, B. Nagarajan, and R. Bürgmann (2007), Coseismic Slip Distributions of the 26 December 2004 Sumatra–Andaman and 28 March 2005 Nias Earthquakes from GPS Static Offsets, *Bull. Seismol. Soc. Am., 97*(1A), S86–S102, doi:10.1785/0120050609.

Bilek, S.L. (2007), Using Earthquake Source Durations along the Sumatra–Andaman Subduction System to Examine Fault-Zone Variations, *Bull. Seismol. Soc. Am., 97*(1A), S62–S70, doi: 10.1785/0120050622.

Bilek, S.L., and T. Lay (1998), Variation of Interplate Fault Zone Properties with Depth in the Japan Subduction Zone, *Science, 281*, 1175-1178, doi:10.1126/science.281.5380.1175.

Bilek, S.L., and T. Lay (1999), Rigidity variations with depth along interplate megathrust faults in subduction zones, *Nature, 400*, 443-446, doi:10.1038/22739.

Bilek, S.L., K. Satake, and K. Sieh (2007), Introduction to the special issue on the 2004 Sumatra-Andaman earthquake and the Indian Ocean tsunami, *Bull. Seismol. Soc. Am.*, *97*, S1 – S5, doi:10.1785/0120050633.

Bilham, R. (2005), A flying start, then a slow slip, *Science*, *308*, 1126-1127, doi:10.1126/science.1113363.

Borrero, J. C. (2005), Field survey of northern Sumatra and Banda Aceh, Indonesia after the tsunami and earthquake of 26 December 2004, *Seism. Res. Lett.*, *76*, 312–320.

Boschi, E., E. Casarotti, R. Devoti, D. Melini, G. Pietrantonio and F. Riguzzi (2006), Coseismic deformation induced by the Sumatra earthquake, *J. Geodyn., 42*, 52-62.

Boschi, L., A. Piersanti and G. Spada (2000), Global postseismic deformation: deep earthquakes, *J. Geophys. Res., 105*, 631-652, doi:10.1029/1999JB900278.

Catherine, J.K., V.K. Gahalaut, and V.K. Sahu (2005), Constraints on rupture of the December 26, 2004, Sumatra earthquake from far-field GPS observations, *Earth Plan. Sc. Lett., 237,* 673-679, doi:10.1016/j.epsl.2005.07.012.

Chlieh, M. et al. (2007), Coseismic slip and afterslip of the Great (Mw9.15) Sumatra-Andaman Earthquake of 2004, *Bull. Seism. Soc. Am., 97*, S152–S173, doi:10.1785/0120050631.

Dow , J.M., R.E. Neilan, and G. Gendt (2005), The International GPS Service (IGS): Celebrating the 10th Anniversary and Looking to the Next Decade, *Adv. Space Res.* 36 vol. 36, no. 3, pp. 320-326, doi:10.1016/j.asr.2005.05.125.

Dragani, W.C., E.E. D'Onofrio, W. Grismeyera, and M.E. Fiore (2006), Tide gauge observations of the Indian ocean tsunami, December 26, 2004, in Buenos Aires coastal waters, Argentina, *Cont. Shelf. Res., 26*, 1543-1550, doi:10.1016/j.csr.2006.03.002.

Dziewonski, A. M., and D. L. Anderson (1981), Preliminary reference Earth model (PREM), *Phys. Earth Planet. Interiors, 25*, 297–356, doi:10.1016/0031-9201(81)90046-7.

Fujii, Y., and K. Satake (2006), Source of the July 2006 West Java tsunami estimated from tide gauge records, Geophys. Res. Lett., 33, L24317, doi:10.1029/2006GL028049.

Fujii, Y., and K. Satake (2007), Tsunami source of 2004 Sumatra-Andaman earthquake inferred from tide-gauges and satellite data, *Bull. Seismol. Soc. Am.*, *97*(1A), S192-S207, doi:10.1785/0120050613.

Fujii, Y., and K. Satake (2008), Tsunami Sources of the November 2006 and January 2007 Great Kuril Earthquakes, *Bull. Seismol. Soc. Am.*, *98*(3), 1559-1571, doi:10.1785/0120070221

Gahalaut, V.K., B. Nagarajan, J.K. Catherine, and S. Kumar (2006), Constraints on 2004 Sumatra–Andaman earthquake rupture from GPS measurements in Andaman–Nicobar Islands, *Earth Plan. Sc. Lett., 242,* 365-374, doi:10.1016/j.epsl.2005.11.051.

Geist, E.L. (1999), Local tsunamis and earthquake source parameters, *Advances in Geophysics*, *39*, 117-209.

Geist, E.L., and S.L. Bilek (2001), Effect of depth-dependent shear modulus on tsunami generation along subduction zones, *Geophys. Res. Lett.*, *28*(7), 1315-1318.

Geist, E.L., V.V. Titov, D. Arcas, F.P. Pollitz, and S.L. Bilek (2007), Implications of the December 26, 2004 Sumatra-Andaman earthquake on tsunami forecast and assessment models for great subduction zone earthquakes, *Bull. Seismol. Soc. Am.*, *97*(1A), S249-S270, doi:10.1785/0120050619.

GGCI. Geodesy and Geodinamics Center of Indonesia.

GLOSS. Global Sea Level Observing System, JCOMM/WMO/IOC UNESCO.

Gower, J. F. (2005), Jason 1 detects December 26, 2004 tsunami, *Eos. Transactions American Geophysical Union*, *86*, 37-38.

Grilli, S. T., M. Ioualalen, J. Asavanant, F. Shi, J. T. Kirby, and P. Watts (2007), Source constraints and model simulation of the December 26, 2004 Indian Ocean tsunami, *J. Waterw. Port Coastal Ocean Eng., 133*(6), 414-428, doi: 10.1061/(ASCE)0733-950X(2007)133:6(414).

Gu, Y. J. (2006), Preface to special issue, *Surv. Geophys., 27*, 601 – 602, doi:10.1007/s10712-006-9014-3.

Hashimoto, M., N. Choosakul, M. Hashizume, S. Takemoto, H. Takiguchi, Y. Fukuda, and K. Fujimori (2006), Crustal deformations associated with the great Sumatra-Andaman earthquake deduced from countinuous GPS observation, *Earth Planets Space*, *58*, 203-209.

HDRTN, Hydrographic Department, Royal Thai Navy, Thailand.

Hébert, H., A. Sladen, and F. Schindelé (2007), Numerical Modeling of the Great 2004 Indian Ocean Tsunami: Focus on the Mascarene Islands, *Bull. Seismol. Soc. Am.*, *97*(1A), S 08–S222, doi: 10.1785/0120050611.

Hirata, K., K. Satake, Y. Tanioka, T. Kuragano, Y. Hasegawa, Y. Hayashi and N. Hamada (2006), The 2004 Indian ocean tsunami: tsunami source model from satellite altimetry, *Earth Planets Space*, *58*, 195-201.

Hoechner A., A. Y. Babeyko, S. V. Sobolev (2008), Enhanced GPS inversion technique applied to the 2004 Sumatra earthquake and tsunami, *Geophys. Res. Lett.*, *35*, L08310, doi:10.1029/2007GL033133.

Ichinose G., P. Somerville, H.K. Thio, R. Graves, and D. O'Connell (2007), Rupture process of the 1964 Prince William Sound, Alaska, earthquake from the combined inversion of seismic, tsunami, and geodetic data, *J. Geophys. Res., 112,* B07306, doi:10.1029/2006JB004728.

IGS, International GNSS Service, http://igscb.jpl.nasa.gov/ (last accessed March 2009).

Ioualalen, M, J. Asavanant, N. Kaewbanjak, S.T. Grilli, J.T. Kirby, and P. Watts (2007), Modeling the 26 December 2004 Indian Ocean tsunami: Case study of impact in Thailand, *J. Geophys. Res., 112,* C07024, doi:10.1029/2006JC003850.

Jade, S., M. Ananda, P. Kumar, and S. Banerjee (2005), Co-seismic and post-seismic displacements in Andaman and Nicobar islands from GPS measurements, *Curr. Sci.,* 88, 1980–1984.

Jaffe, B. E., et al. (2006), Northwest Sumatra and Offshore Islands Field Survey after the December 2004 Indian Ocean tsunami, *Earthquake Spectra*, *22*, S105–S135.

Ji, C., D.J. Wald, D.V. Helmberger (2002), Source description of the 1999 Hector Mine, California earthquake; Part I: wavelet domain inversion theory and resolution analysis, *Bull. Seismol. Soc. Am.*, *92*, 4, 1192-1207,doi:10.1785/0120000916.

Joseph A., J.T. Odametey, E.K. Nkebi, A. Pereira, R.G. Prabhudesai, P. Mehra, A.B. Rabinovich, V. Kumar, S. Prabhu- desai and P. Woodworth (2006), The 26 December 2004 Sumatra tsunami recorded on the coast of West Africa, *Afr. J. Mar. Sci., 28*(3&4), 705–712.

Kennett, B.L.N., and P.R. Cummins (2005), The relationship of the seismic source and subduction zone structure for the 2004 December 26 Sumatra-Andaman earthquake, *Earth Plan. Sc. Lett., 239*, 1-8, doi:10.1016/j.epsl.2005.08.015.

Lay, T. et al. (2005), The great Sumatra-Andaman earthquake of 26 December 2004, *Science*, *308*, 1127-1133, doi:10.1126/science.1112250.

Lorito, S., A. Piatanesi, and A. Lomax (2008a), Rupture Process of the 18 April 1906 California Earthquake from Near-Field Tsunami Waveform Inversion, *Bull. Seismol. Soc. Am., 98*(2), 832–845, doi: 10.1785/0120060412.

Lorito, S., F. Romano, A. Piatanesi, and E. Boschi (2008b), Source process of the September 12, 2007, Mw 8.4 southern Sumatra earthquake from tsunami tide gauge record inversion, *Geophys. Res. Lett.*, *35*, L02310, doi:10.1029/2007GL032661.

Mader, C. L. (2001), *Numerical Modeling of Water Waves*, Los Alamos Ser. 341 Basic Appl. Sci., vol. 8, CRC Press, Boca Raton, Fla.

Marks, K.M., and W.H.F. Smith (2006), An evaluation of publicly available bathymetry grids, *Mar. Geophys. Res., 27*, 19-34.

Masterlark, T., and K.L. Hughes (2008) The next generation of deformation models for the 2004 M9 Sumatra-Andaman Earthquake, *Geophys. Res. Lett, 35*, L19310, doi:10.1029/2008GL035198.

Megna, A., S. Barba, S. Santini, and M. Dragoni (2008), Effects of geological complexities on coseismic displacement: hints from 2D numerical modelling, *Terra Nova*, *20*(3), 173-179, doi:10.1111/j.1365-3121.2008.00800.x.

Menke, W., H. Abend, D. Bach, K. Newman, and V. Levin (2006), Review of the source characteristics of the Great Sumatra–Andaman Islands earthquake of 2004, *Surv Geophys, 27*, 603–613, doi: 10.1007/s10712-006-9013-4.

Merrifield, M.A. et al. (2005), Tide gauge observations of the Indian Ocean tsunami, December 26, 2004, *Geophys. Res. Lett.*, *32*, L09603, doi:10.1029/2005GL022610.

Nagarajan, B., I. Suresh, D. Sundar, R. Sharma, A.K. Lal, S. Neetu, S.S.C. Shenoi, S.R Shetye, and D. Shankar (2006), The great tsunami of 26 December 2004: a description based on tide-gauge data from the Indian subcontinent and surrounding areas, *Earth Planet Space, 58*, 211–215.

NIO. National Institute of Oceanography, Goa, India.

Obura, D. (2006), Impacts of the 26 December 2004 tsunami in Eastern Africa, *Ocean Coast. Manage.*, *49*, 873–888, doi:10.1016/j.ocecoaman.2006.08.004.

Okada, Y. (1992), Internal deformation due to shear and tensile faults in a half-space, *Bull. Seismol. Soc. Am.*, *82*, 1018-1040.

Piatanesi, A., A. Cirella, P. Spudich and M. Cocco (2007) : A global search inversion for earthquake kinematic rupture history : application to the 2000 Western Tottori, Japan earthquake *J. Geophys. Res.* Vol. 112, No. B7, B07314, doi:10.1029/2006JB004821.

Piatanesi, A., and S. Lorito (2007), Rupture Process of the 2004 Sumatra–Andaman Earthquake from Tsunami Waveform Inversion, *Bull. Seismol. Soc. Am.*, *97*(1A), S223-S231, doi: 10.1785/0120050627.

Piersanti, A., G. Spada, R. Sabadini, and M. Bonafede (1995), Global post-seismic deformation, *Geophys. J.Int., 120,* 544–566, doi:10.1111/j.1365-246X.1995.tb01838.x.

Pietrzak, J., A. Socquet, D. Ham, W. Simon, C. Vigny, R. J. Labeur, E. Schrama, G. Stelling, and D. Vatvani (2007), Defining the source region of the Indian Ocean Tsunami from GPS, altimeters, tide gauges and tsunami models, *Earth Planet. Sci. Lett., 261*, 49-64, doi:10.1016/j.epsl.2007.06.002.

PO.DAAC. Physical Oceanography Distributed Active Archive Center, Jet Propulsion Laboratory Caltech/NASA, USA.

Rabinovich A.B., R.E. Thomson, and F.E. Stephenson (2006), The Sumatra tsunami of 26 December 2004 as observed in the North Pacific and North Atlantic oceans, *Surv. Geophys., 27*, 647–677, doi:10.1007/s10712-006-9000-9.

Rabinovich A.B., and R.E. Thomson (2007), The 26 December 2004 Sumatra Tsunami: Analysis of Tide Gauge Data from the World Ocean Part 1. Indian Ocean and South Africa, *Pure Appl. Geophys., 164*, 261–308, doi:10.1007/s00024-006-0164-5.

Rhie, J., D. Dreger, R. Bürgmann, and B. Romanowicz (2007), Slip of the 2004 Sumatra–Andaman Earthquake from Joint Inversion of Long-Period Global Seismic Waveforms

and GPS Static Offsets, *Bull. Seismol. Soc. Am.*, *97*(1A), S115-S127, doi: 10.1785/0120050620.

Rothman, D. (1986), Automatic estimation of large residual statics corrections, *Geophysics*, *51*, 332-346.

Sambridge M., J. Braun and H. McQueen (1995), Geophysical parameterization and interpolation of irregular data using natural neighbours, *Geophys. J.Int.*, *122*, 837-857, doi:10.1111/j.1365-246X.1995.tb06841.x

Satake, K. , E.A. Okal, and J. C. Borrero (2007), Tsunami and its Hazard in the Indian and Pacific Oceans: Introduction, *Pure Appl. Geophys., 154*(2-3), 249-259, doi: 10.1007/s00024-006-0172-5.

Sen, M. and Stoffa P.L. (1991), Nonlinear one-dimensional seismic waveform inversion using simulated annealing, *Geophysics*, *56*, 1624-1638.

Seno, T. and K. Hirata (2007), Did the 2004 Sumatra–Andaman Earthquake Involve a Component of Tsunami Earthquakes? *Bull. Seismol. Soc. Am.*, *97*(1A), S296 - S306, doi: 10.1785/0120050615.

Shapiro, N.M., M.H. Ritzwoller, and E.R. Engdahl (2008) Structural context of the great Sumatra-Andaman Islands earthquake, *Geophys. Res. Lett.*, *35*, L05301, doi:10.1029/2008GL033381.

Sindhu B, I. Suresh, A.S. Unnikrishnan, N.V. Bhatkar, S. Neetu, and G.S. Michael (2007), Improved bathymetric datasets for the shallow water regions in the Indian Ocean, *J. Earth Syst. Sci.*, *116*(3), 261-274, doi: 10.1007/s12040-007-0025-3.

Sladen A., and H. Hébert (2008), On the use of satellite altimetry to infer the earthquake rupture, characteristics: application to the 2004 Sumatra event, *Geophys. J.Int.*, *172*, 707–714, doi: 10.1111/j.1365-246X.2007.03669.x

Smith, W. H. F., and P. Wessel (1990), Gridding with continuous curvature splines in tension, *Geophysics*, *55*, 293−305.

Smith, W.H.F., R. Scharroo, V. V. Titov, D. Arcas , and B. K. Arbic (2005), Satellite Altimeters Measure Tsunami, *Oceanography, 18*, 11-13.

Soldati, G., A. Piersanti, A., and E. Boschi (1998), Global postseismic gravity changes of a viscoelastic Earth*, J. Geophys. Res., 103,* 29,867-29,885, doi:10.1029/98JB02793.

Spudich, P. and D.P. Miller (1990), Seismic site effects and the spatial interpolation of earthquake seismograms: results using aftershocks of the 1986 North Palm Springs, California earthquake, *Bull. Seismol. Soc. Am., 80*, 1504-1532.

Stein, S., and E. A. Okal (2005), Speed and size of the Sumatra earthquake, *Nature*, *434*, 581-582, doi:10.1038/434581a.

Subarya, C., M. Chlieh, L. Prawirodirdjo, J-P. Avouac, Y. Boch, K. Sieh, A.J. Meltzmer, D.H. Natawidjaja and R. McCaffrey (2006), Plate-boundary deformation associated with the great Sumatra-Andaman earthquake, *Nature, 440,* 46-51, doi:10.1038/nature04522.

SuGAr, Sumatran GPS Array of Caltech's Tectonics Observatory, http://www.tectonics.caltech.edu/sumatra/data.html (last accessed March 2009).

Tanioka, Y., E.L. Geist, and N.T. Puspito (2006a), Preface to special issue ''The 2004 Great Sumatra Earthquake and Tsunami'', *Earth Planets Space 58(2),* 111.

Tanioka, Y., Yudhicara, T. Kususose, S. Kathiroli, Y. Nishimura, S.I. Iwasaki, and K. Satake (2006b), Rupture process of the 2004 great Sumatra-Andaman earthquake estimated from tsunami waveforms, *Earth Planet Space, 58*, 203-209.

Tinti, S., and R. Tonini (2005), Analytical evolution of tsunamis induced by near-shore earthquakes on a constant-slope ocean, *J. Fluid Mech., 535*, 33–64, doi:10.1017/S0022112005004532.

Titov, V., A.B. Rabinovich, H.O. Mofjeld, R.E. Thomson, and F.I. González (2005), The Global Reach of the 26 December 2004 Sumatra Tsunami, *Science, 309*, 2045-2048, doi:10.1126/science/1114576.

Thomson R.E. , A.B. Rabinovich, and M.V. Krassovski (2007), Double jeopardy: Concurrent arrival of the 2004 Sumatra tsunami and storm-generated waves on the Atlantic coast of the United States and Canada, *Geophys. Res. Lett.*, *34*, L15607, doi:10.1029/2007GL030685.

Tsuji, Y., H. Matsutomi, Y. Tanioka, Y. Nishimura, T. Sakakiyama, T., Kamataki, Y. Murakami, A. Moore, and G. Gelfenbaum (2005), Distribution of the tsunami heights of the 2004 Sumatera tsunami in Banda Aceh measured by the Tsunami Survey Team, edited, University of Tokyo, http://www.eri.u-tokyo.ac.jp/namegaya/sumatera/surveylog/eindex.htm (last accessed March 2009).

Tsuji, Y., Y. Namegaya, H. Matsumoto, S.-I. Iwasaki, W. Kambua, M. Sriwichai and V. Meesuk (2006), The 2004 Indian tsunami in Thailand: tsunami height and tide-gauge records, *Earth Planet Space*, *58*, 223-232.

UHSLC. University of Hawaii Sea Level Center, USA.

Vigny, C., W.J.F. Simons, S. Abu, R. Bamphenyu, C. Satirapod, N. Choosakul, C. Subaraya, A. Soquet, K. Omar, H.Z. Abidin and B.A.C. Ambrosius (2005), GPS in SE Asia provides unforeseen insights on the 2004 megathrust earthquake Insight into the 2004 Sumatra-Andaman earthquake from GPS measurements in Southeast Asia, *Nature*, *436*, 201-206, doi:10.1038/nature03937.

Wang, R., F. L. Lorenzo, and F. Roth (2003). Computation of deformation induced by earthquakes in multi-layered elastic crust — FORTRAN programs EDGRN/EDCMP, *Comput. Geosci.*, *29*, 195–207.

Wessel, P., and W.H.F. Smith (1998), New, improved version of the Generic Mapping Tools released, *EOS Trans. AGU, 79*, 579.

Zhao, S., R.D. Müller, Y. Takahashi, and Y. Kaneda (2004), 3-D finite-element modelling of deformation and stress associated with faulting: effect of inhomogeneous crustal structures, *Geophys. J. Int., 157,* 629-644, doi:10.1111/j.1365-246X.2004.02200.x.

Figure captions

Figure 1. Map of the computational domain for the tsunami propagation. The star indicates the position of the Sumatra 2004 earthquake epicenter. Thin black lines mark the surface projection of the subfaults used in this study. Red triangles show the locations of tide-gages stations used in the inversions. The black and red lines are the projections at the sea surface of the altimetric satellites tracks portions used in the inversions. The magenta dots show the GPS stations used in the inversion, falling in the tsunami computational domain. Gray rectangles are the borders of the nautical charts we digitized (cf. Tab. 2).

Figure 2. Checkerboard (resolution) test for the tsunami dataset, i.e. the tide-gage and the satellite altimeter data. The free inversion parameters are slip, rake, and rupture velocity. The target checkerboard model is shown in the left panel, and the best model retrieved by the inversion in the right panel. The target slip distribution, with alternating 5 and 15 meters values is represented by the subfault color. Rake directions are indicated by blue arrows, rupture velocities by the numbers besides the black arrows at both sides of the fault. The checkerboard slip pattern of the target model is recovered fairly well, as well as the rake and the rupture velocities. Numerical values of all inverted parameters (slip, rake and velocity) are reported in Table 5, columns 2-3.

Figure 3. Checkerboard (resolution) test for the geodetic dataset. The free inversion parameters are slip and rake. Colors and symbols are as described in caption of Figure 2, with exception for the velocity, that is not inverted by static data. The checkerboard slip pattern (left panel) is totally missed in the best model (right panel), while the rake is

correctly recovered with the exception of the northernmost subfaults. Numerical values of all inverted parameters (slip, rake) are reported in Table 5, columns 4-5.

Figure 4. Resolution test for the geodetic dataset, with the target model featuring broader patches of slip (left panel); see also caption of Figure 3. In this case, with a lower spatial resolution on the slip distribution, the geodetic dataset is sufficient to recover the alternating slip pattern (see the best model in the right panel), even if the resolution further degrades in the northernmost stretch, where both slip and rake are partially missed. Numerical values of all inverted parameters (slip, rake) are reported in Table 5, columns 6-7.

Figure 5. Checkerboard (resolution) test for the joint inversion of the tsunami and geodetic datasets. The free parameters in the joint inversion are: slip, rake, velocity, and rigidity. Gray ellipses under the source zone highlight that in the present case we have the rigidity as an extra free parameter. For a description of other colors and symbols see caption of Figure 2. The target model configuration is depicted in the left panel. The checkerboard slip pattern is recovered fairly well (best model shown in the right panel). Numerical values of the slip, rake, velocity, and rigidity featured by the best model are reported in the last two columns of Table 5.

Figure 6. Best (left) and average (right) models for the 2004 Sumatran earthquake, as recovered by the joint inversion of the tsunami and geodetic datasets. Gray ellipses under the source zone highlight that in the present case we have the rigidity as an extra free parameter. Numerical values for the slip, rake, velocity and rigidity are reported in

Table 6. The values featured by the best model are listed in columns 1 and 2; those of the average model, with their associated errors, in columns 3 and 4.

Figure 7. Comparison between the experimental and synthetic datasets obtained with the best source model for the 2004 earthquake. Tide-gage and satellite tsunami records are represented with red lines; their synthetic counterparts with black lines. Red arrows (with error ellipses) show the geodetic data, and black arrows their synthetic counterparts.

Figure 8. Comparison between the experimental and synthetic datasets obtained here with the average source model for the 2004. See also caption of Figure 7.

Figure 9. Comparison between the forward predictions of our best model (black arrows) with the geodetic (campaign) data in the near-field, represented by red arrows with error circles. The model under-predicts the data, particularly over the Andaman and Nicobar islands, and even in the Northern part of Sumatra.

Table 1. Tide gage stations list.

Station	Lat	Lon	a/d (*)	Sampling (min)	Weight
Krabi	08.05 N	98.92 E	a	5	0.75
Tarutao	06.70 N	99.65 E	a	5	0.75
Ranong	09.95 N	98.58 E	a	5	0.75
Ta pao	07.77 N	98.42 E	a	5	0.75
Sibolga	01.75 N	98.77 E	d	10	0.5
Diego garcia	07.28 S	72.40 E	d	6	0.75
Gan	00.68 S	73.15 E	d	4	1
Male	04.18 N	73.52 E	d	4	1
Hanimaadhoo	06.76 N	73.17 E	d	2	1
Visakhapatnam	17.68 N	83.28 E	d	5	0.75
Paradip	20.26 N	86.70 E	d	6	0.75
Chennai	13.10 N	80.30 E	d	5	0.75
Tuticorin	08.80 N	78.15 E	d	6	0.75

(*) a= analogical, d=digital

Table 2. Digitized charts list.

N°	Title	North	East	South	West	Scale
3	Chagos Archipelago	4.58S	72.83E	7.83S	70.65E	1:360000
400	Ujung Karang to Sibolga	4.17N	99.00E	1.22N	94.58E	1:500000
813	Colombo to Sangama Kanda Point	7.11N	82.17E	5.30N	78.93E	1:300000
814	The Sandheads - Paradip to Raimangal River	21.86N	89.34E	20.17N	86.58E	1:300000
825	Andaman Islands	15.33N	94.50E	10.03N	91.50E	1:500000
840	Little Andaman to Great Nicobar	10.83N	94.51E	6.25N	91.50E	1:500000
842	Chowra to Great Nicobar	8.59N	93.96E	6.74N	92.93E	1:175000
920	Diego Garcia	7.19S	72.50E	7.45S	72.35E	1:25000
1011	Addoo Atoll to North Huvadhoo Atoll	1.17N	74.00E	1.50S	72.20E	1:300000
1013	Mulaku Atoll to South Maalhosmadulu Atoll	5.33N	74.00E	2.67N	72.20E	1:300000
1014	South Maalhosmadulu Atoll to Ihavandhippolhu Atoll	7.45N	74.00E	4.80N	72.20E	1:300000
1509	Coondapoor to Vengurla	16.07N	74.75E	13.33N	72.95E	1:300000
1564	Sacrifice Rock to Coondapoor	14.02N	75.79E	11.25N	73.99E	1:300000
1565	Alleppey to Sacrifice Rock	11.75N	76.56E	8.97N	74.75E	1:300000
1566	Cape Comorin to Cochin	10.00N	77.58E	7.20N	75.78E	1:300000
1583	Little Basses Reef to Pulmoddai Roads	9.12N	82.47E	6.37N	80.67E	1:300000
1584	Trincomalee to Point Calimere	10.33N	81.67E	8.52N	78.88E	1:300000
1586	Pamban to Cape Comorin	9.50N	80.00E	7.73N	77.24E	1:300000
1587	Colombo to Cape Comorin	8.20N	80.00E	6.43N	77.24E	1:300000
2058	Puri to the Sandheads	21.22N	88.42E	19.55N	85.67E	1:300000
2060	Kalingapatnam to Puri	19.93N	86.77E	18.25N	84.00E	1:300000
2061	Kakinada to Kalingapatnam	18.52N	84.97E	16.82N	82.20E	1:300000
2062	False Divi Point to Kakinada	17.13N	83.17E	15.42N	80.17E	1:300000
2063	Madras to False Divi Point	15.83N	81.78E	12.92N	80.00E	1:300000
2067	Addoo Atoll	0.57S	73.27E	0.72S	73.04E	1:25000
2069	Point Calimere to Madras	13.17N	81.42E	10.08N	79.58E	1:300000
2777	Indira Point to Teluk Aru and Ujung Kareueng	6.83N	98.70E	3.90N	93.52E	1:500000
2779	Pulau Ilir to Pulau Nyamuk	1.37N	100.83E	1.50S	96.50E	1:500000
3052	Za Det Gyi Island to Mu Ko Similan	10.15N	98.67E	8.36N	97.50E	1:200000
3323	Male' Atoll	4.82N	73.88E	3.95N	73.17E	1:150000
3941	Mu Ko Similan to Ko Lanta Yai	8.56N	99.37E	7.39N	97.61E	1:200000
3942	Ko Lanta Yai to Ko Tarutao	7.60N	100.14E	6.43N	98.30E	1:200000
3943	Ko Tarutao to Pulau Pinang	6.59N	100.43E	5.45N	98.60E	1:200000

Table 3. Geodetic dataset used in this study. Data from *Banerjee et al.*, [2007] and references therein.

Lon	Lat	E_{offset}	N_{offset}	E_{sig}	N_{sig}	Site
°E	°N	mm	mm	mm	mm	
99.39	0.22	-4.22	-5.11	3.66	2.32	ABGS
100.28	6.45	-130.25	-33.76	9.14	4.05	ARAU
106.84	-6.49	0.06	-5.84	3.67	2.27	BAKO
77.51	13.03	11.18	-3.34	4.11	2.68	BAN2
78.6	30.8	0.89	-1.45	2.86	1.97	BHTW
85.8	20.3	7.22	-4.26	8.47	4.18	BHUB
100.61	13.67	-60.93	-42.55	4.26	2.61	BNKK
115.89	39.61	-4.6	-4.99	3.94	2.92	BJFS
98.97	18.77	-15.8	-24.9	4.89	2.96	CHMI
98.9	18.8	-14.04	-25.84	6.95	3.89	CMU
96.83	-12.19	4.63	-0.77	3.72	2.22	COCO
99.4	10.7	-127.39	-67.47	4.37	2.53	CPN
127.37	36.4	-2.34	-6.02	3.96	3.1	DAEJ
72.37	-7.27	6.73	-0.71	3.98	2.24	DGAR
78.55	17.42	6.8	-4.37	2.95	1.95	HYDE
77.57	13.02	12.34	-2.42	3	1.96	IISC
117.1	-20.98	-3.28	1.36	4.59	2.63	KARR
66.89	39.13	-1.53	-3.08	2.23	1.57	KIT3
100.8	13.7	-56.4	-44.26	5.1	3.08	KMI
103.14	5.32	-56.67	-5.59	7.69	4.12	KUAL
102.8	25.03	-4.66	-8.52	3.54	2.39	KUNM
91.1	29.66	-1.09	-2.76	4.45	2.87	LHAS
101.16	-2.29	5.53	-4.05	4.27	2.46	LNGG
80.9	26.9	0.1	-1.84	3.91	2.35	LUCK
101.09	-2.54	6.06	-5.93	4.37	2.47	MKMK
99.09	-1.33	2.85	-8.54	3.64	2.29	MSAI
76.3	32.2	1.76	0.61	3.26	2.01	NADI
99.27	-1.8	1.58	-7.94	3.99	2.36	NGNG
103.68	1.35	-14.62	1.65	3.22	2.22	NTUS
98.53	-0.03	-6.29	-0.69	18.19	4.73	PBAI
98.31	8.11	-239.3	-107.72	4.62	2.56	PHKT
121.08	14.64	-10.73	-5.49	3.89	2.55	PIMO
74.69	42.68	-4.32	2.93	2.59	1.89	POL2
100.4	-2.97	1.28	-7.23	4.31	2.42	PRKB
77.5	23.2	0.71	-3.58	4.1	2.34	RRLB
98.72	3.62	-132.52	-19.05	5.41	2.5	SAMP
91.9	25.6	-1.24	-2.45	4.43	2.68	SHL2
99.867	17.157	-30.4	-32.14	4.22	2.6	SIS2
127.05	37.28	-5.91	-3.02	4.17	3.28	SUWN
77	8.4	16.49	-1.86	10.07	3.76	TIR0
120.99	24.8	-10.39	-2.42	4.1	2.84	TNML
78	30.3	0.69	-1.11	2.74	1.9	WIH2
114.36	30.53	-6.02	-4.68	4.51	3.04	WUHN
101.52	3.77	-55.91	2.31	2.79	1.88	BEHR
113.07	3.26	-10.39	-6.17	5.18	2.32	BINT
116.04	5.91	-5.78	-0.21	4.84	2.2	KINA
103.35	3.83	-39.16	1.06	3.74	2.19	KUAN

115.25	5.28	-8.18	-2.7	4.58	2.1	LABU
119.91	-0.92	-1.18	0.13	4.21	1.75	PALP
121.2	31.1	-2.9	-0.38	5.11	4.84	SHAO
120.1	-0.71	1.51	0.75	5.09	2.15	TOBP
116.83	-1.27	-3.65	-0.51	4.71	1.92	UNO0
100.3	5.36	-115.13	-14.41	4.78	2.9	USMP
119.59	-0.87	-1.53	-0.98	4.29	1.8	WATP
103.64	1.57	-19.51	4.55	3.69	2.15	UTMJ
101.54	2.83	-45.01	3.47	3.93	2.45	BANT
101.96	4.86	-70.52	-2.37	4.58	3.03	GMUS
101.13	5.44	-90.92	-10.88	3.68	2.57	GRIK
103.8	1.54	-17.92	3.81	3.93	2.35	JHJY
101.09	4.6	-77.49	-1.93	3.59	2.48	JUIP
102.26	2.21	-27.73	5.23	3.81	2.35	JUML
101.66	3.56	-52.12	1.04	3.97	2.65	KKBH
103.32	2.03	-22.92	3.58	4.13	2.46	KLUG
103.45	1.33	-17.02	3.76	4.15	2.55	KUKP
99.85	6.33	-148.87	-34.99	3.51	2.73	LGKW
103.83	2.45	-26.65	3.08	4.37	2.63	MERS
101.41	3.14	-50.37	2.32	3.99	2.61	MERU
103.39	3.49	-35.15	1.71	4.06	2.56	PEKN
100.56	4.21	-85.62	-1.84	3.96	2.55	PUPK
100.7	5.22	-102.29	-11.99	3.54	2.54	SELM
100.49	5.64	-116.43	-14.03	3.5	2.64	SGPT
104.11	1.37	-16.18	3.84	3.95	2.31	TGPG
102.42	3.45	-41.55	1.49	4.6	3.16	TLOH
101.72	2.99	-42.63	4.54	4.41	2.77	UPMS
100.51	6.46	-122.47	-23.1	4.26	3.12	UUMK
118.12	5.84	-9.5	-6.02	8.22	3.37	SAND
117.88	4.26	-5.64	1.98	9.8	3.73	TAWX
99.08	10.61	-155.07	-74.82	3.95	2.37	BANH
101.05	13.12	-68.36	-38.35	2.65	2.03	CHON
100.12	15.67	-39.38	-44.04	4.12	2.75	NAKH
98.3	7.76	-252.5	-101.93	2.49	1.85	PHUK
101.03	12.76	-74.28	-37.1	2.36	1.81	RYNG
104.42	14.9	-32.64	-18	3.03	2.18	SRIS
100.01	15.38	-47.15	-39.54	2.36	1.92	UTHA

Table 4. Subfaults, listed – and counted – from South to North along the source zone.

Fault segment	LONG(*) E	LAT(*) N	W (km)	L (km)	Strike (deg)	Dip (deg)	Top (km)
1 deep	95.845	2.671	113.728	137.154	301.80	13.22	10.1
1 shallow	95.210	1.915	110.273	137.211	301.80	5.20	0.1
2 deep	94.964	3.312	113.624	109.662	309.14	13.23	10.1
2 shallow	94.300	2.583	110.137	123.126	309.50	5.21	0.1
3 deep	94.183	4.206	111.504	125.250	328.16	13.48	10.1
3 shallow	93.400	3.667	106.331	158.965	329.90	5.40	0.1
4 deep	93.582	5.473	103.985	182.400	336.16	14.48	10.1
4 shallow	92.850	5.133	90.568	183.497	341.05	6.34	0.1
5 deep	93.084	7.051	101.266	163.410	342.91	14.88	10.1
5 shallow	92.350	6.750	89.367	172.928	341.39	6.42	0.1
6 deep	92.524	8.416	101.569	176.108	334.56	14.83	10.1
6 shallow	91.733	8.1667	93.561	181.210	334.66	6.14	0.1
7 deep	92.089	10.085	98.863	167.488	357.33	15.25	10.1
7 shallow	91.312	10.075	88.300	204.321	0.77	6.50	0.1
8 deep	92.259	11.637	95.999	156.887	10.71	15.71	10.1
8 shallow	91.562	11.750	80.698	166.563	12.08	7.12	0.1
9 deep	92.602	13.067	92.323	167.403	15.94	16.36	10.1
9 shallow	91.988	13.250	73.763	172.847	17.23	7.79	0.1

(*) Longitude and latitude refer to central point on the upper edge of each subfault.

Table 5. Best model parameters values for the resolution (checkerboard) tests. Target values are in brackets. Subfaults are counted from South to North.

Subfault	T.G.+SAT		GPS		GPS Bigger patches		JOINT	
	Slip (m)	***Rake (deg)***	***Slip (m)***	***Rake (deg)***	***Slip (m)***	***Rake (deg)***	***Slip (m)***	***Rake (deg)***
1 deep	**4***(5)*	**90***(90)*	**10***(5)*	**90***(90)*	**4***(5))*	**95***(90)*	**4***(5)*	**90***(90)*
1 shallow	**16***(15)*		**12***(15)*				**14***(15)*	
2 deep	**15***(15)*		**1***(15)*				**16***(15)*	
2 shallow	**5***(5)*		**2***(5)*				**7***(5)*	
3 deep	**5***(5)*		**20***(5)*				**6***(5)*	
3 shallow	**14***(15)*		**4***(15)*				**15***(15)*	
4 deep	**16***(15)*	**130***(130))*	**11***(15)*	**130***(130))*	**15***(15)*	**130***(130)*	**16***(15)*	**135***(130)*
4 shallow	**5***(5)*		**7***(5)*				**4***(5)*	
5 deep	**5***(5)*		**21***(5)*				**6***(5)*	
5 shallow	**15***(15)*		**0***(15)*				**16***(15)*	
6 deep	**16***(15)*		**8***(15)*				**17***(15)*	
6 shallow	**4***(5)*		**27***(5)*				**5***(5)*	
7 deep	**5***(5)*	**90***(90)*	**5***(5)*	**110***(90)*	**9***(5)*	**100***(90)*	**5***(5)*	**90***(90)*
7 shallow	**14***(15)*		**7***(15)*				**14***(15)*	
8 deep	**16***(15)*		**13***(15)*				**15***(15)*	
8 shallow	**6***(5)*		**24***(5)*				**7***(5)*	
9 deep	**5***(5)*		**6***(5)*				**5***(5)*	
9 shallow	**16***(15)*		**1***(15)*				**16***(15)*	
	Vel. (km/s)						***Vel. (km/s)***	***Rigid. (GPa)***
Subf. 1-4 (shall.)	**1.50***(1.50)*						**1.50***(1.50)*	**30***(30)*
Subf. 1-4 (deep)	**2.50***(2.50)*						**2.50***(2.50)*	
Subf. 5-9 (shall.)	**1.00***(1.00)*						**1.00***(1.00)*	**10***(10)*
Subf. 5-9 (deep)	**2.25***(2.00)*						**2.00***(2.00)*	

Table 6. Best and average models for the 2004 Sumatran earthquake source from the joint inversion of tide-gage, satellite, and GPS data.

Subfault	BEST		AVERAGE	
	Slip (m)	***Rake (deg)***	***Slip (m)***	***Rake (deg)***
1 deep	**1**	**95**	**7±7**	**94±4**
1 shallow	**21**		**21±7**	
2 deep	**34**		**30±4**	
2 shallow	**0**		**4±5**	
3 deep	**22**		**23±4**	
3 shallow	**33**		**30±5**	
4 deep	**8**	**95**	**8±2**	**104±12**
4 shallow	**16**		**17±5**	
5 deep	**3**		**4±3**	
5 shallow	**0**		**5±5**	
6 deep	**12**		**13±4**	
6 shallow	**18**		**15±7**	
7 deep	**3**	**135**	**3±3**	**125±11**
7 shallow	**1**		**4±5**	
8 deep	**8**		**11±6**	
8 shallow	**0**		**4±6**	
9 deep	**6**		**8±6**	
9 shallow	**0**		**4±6**	
	Velocity (km/s)	***Rigidity (GPa)***	***Velocity (km/s)***	***Rigidity (GPa)***
First half of the rupture (shallow)	**2.00**	**20**	**1.9±0.3**	**20±2**
First half of the rupture (deep)	**3.25**		**3.3±0.2**	
Second half of the rupture (shallow)	**0.50**	**30**	**0.9±0.7**	**25±7**
Second half of the rupture (deep)	**2.00**		**2.2±0.7**	

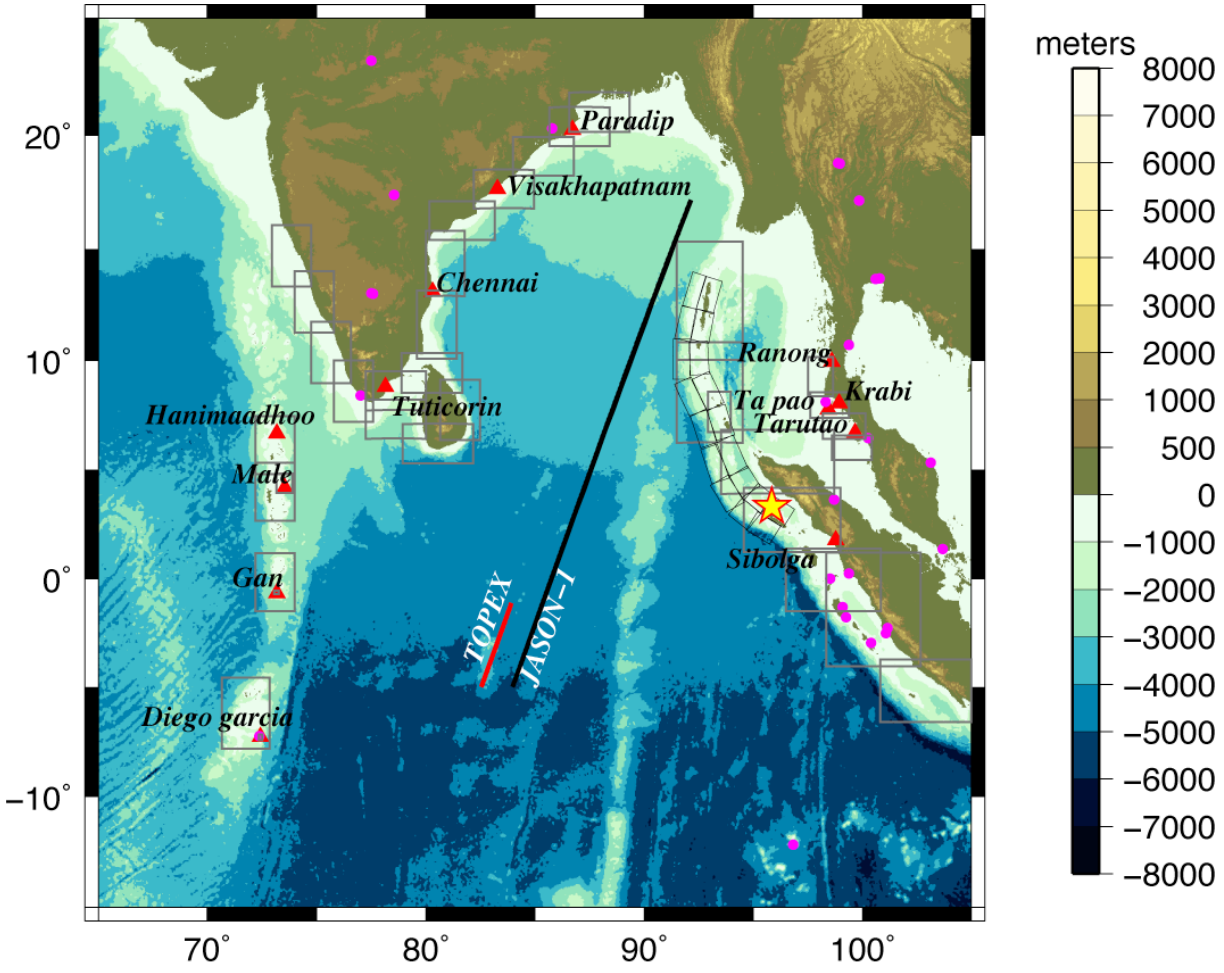
Paradip
Visakhapatnam
Chennai
Tuticorin
Hanimaadhoo
Male
Gan
Diego garcia
Ranong
Ta pao
Krabi
Tarutao
Sibolga
TOPEX
JASON-1
20°
10°
0°
−10°
70°
80°
90°
100°
meters
8000
7000
6000
5000
4000
3000
2000
1000
500
0
−1000
−2000
−3000
−4000
−5000
−6000
−7000
−8000

FIGURE 1

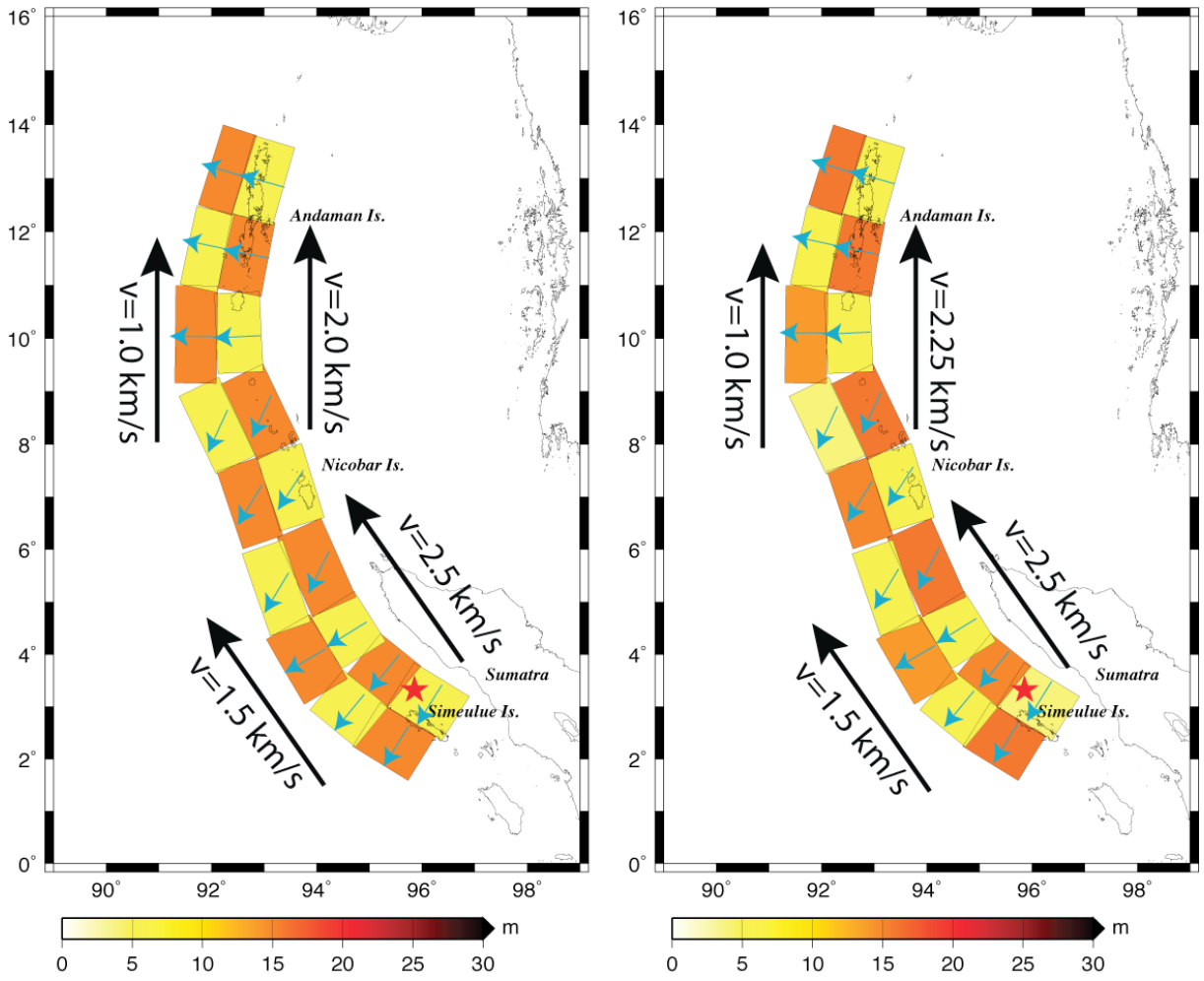
Andaman Is.
Nicobar Is.
Sumatra
Simeulue Is.
v=1.0 km/s
v=2.0 km/s
v=2.5 km/s
v=1.5 km/s
v=2.25 km/s
m
0 5 10 15 20 25 30
90° 92° 94° 96° 98°
0° 2° 4° 6° 8° 10° 12° 14° 16°

FIGURE 2

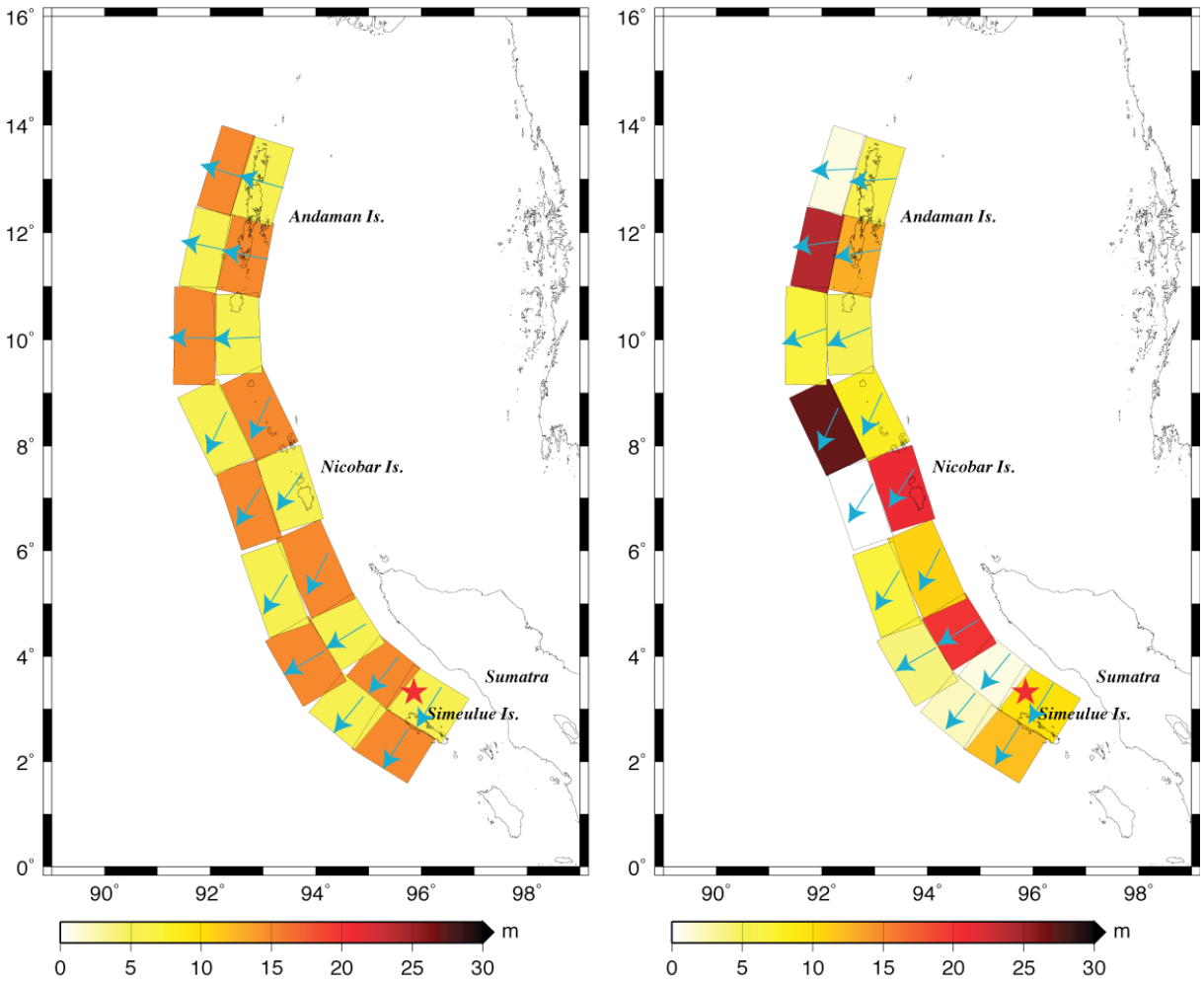
Andaman Is.
Nicobar Is.
Sumatra
Simeulue Is.
m
0 5 10 15 20 25 30
90° 92° 94° 96° 98°
0° 2° 4° 6° 8° 10° 12° 14° 16°

FIGURE 3

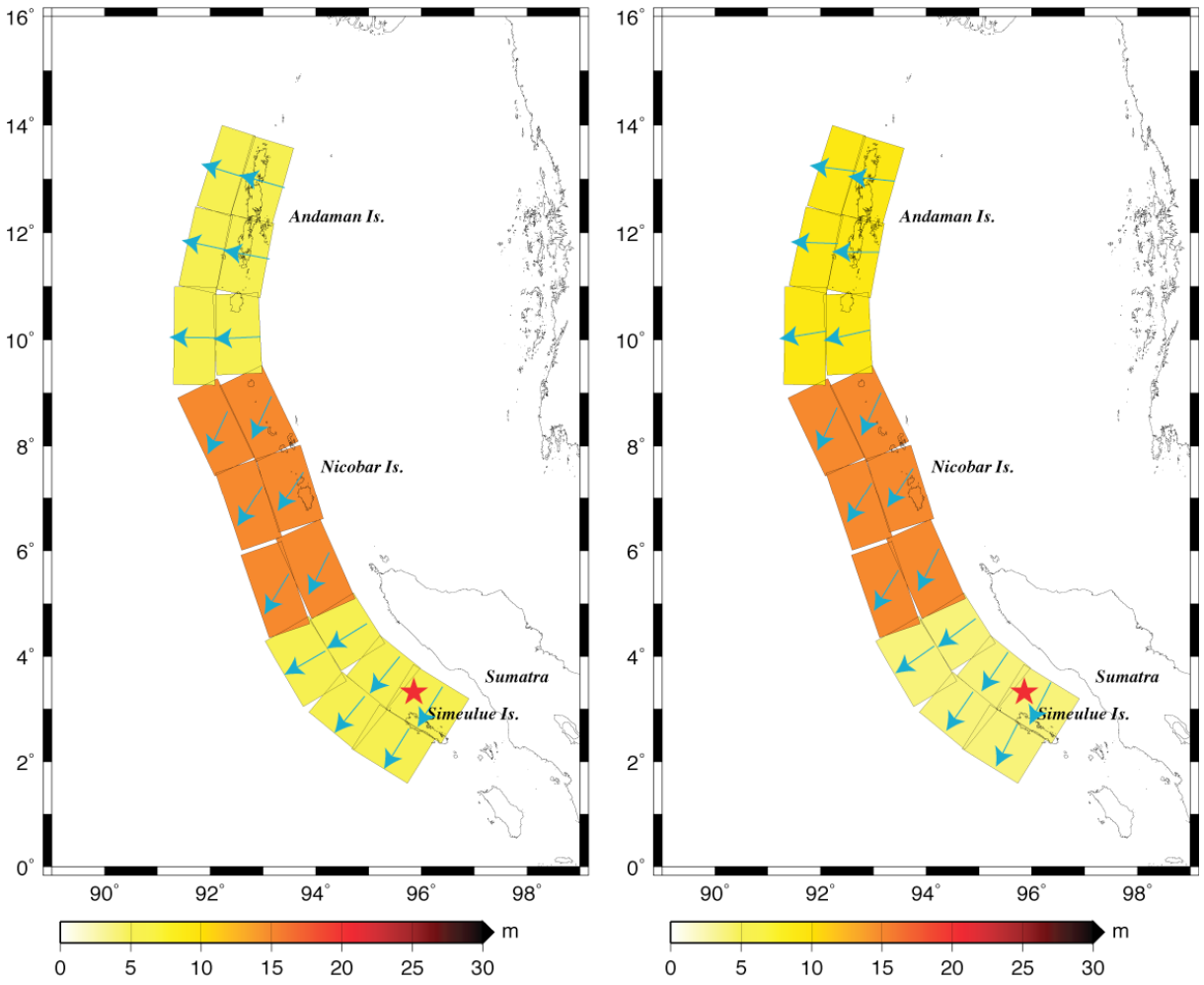
16°
14°
12°
10°
8°
6°
4°
2°
0°
90°
92°
94°
96°
98°
Andaman Is.
Nicobar Is.
Sumatra
Simeulue Is.
m
0
5
10
15
20
25
30

FIGURE 4

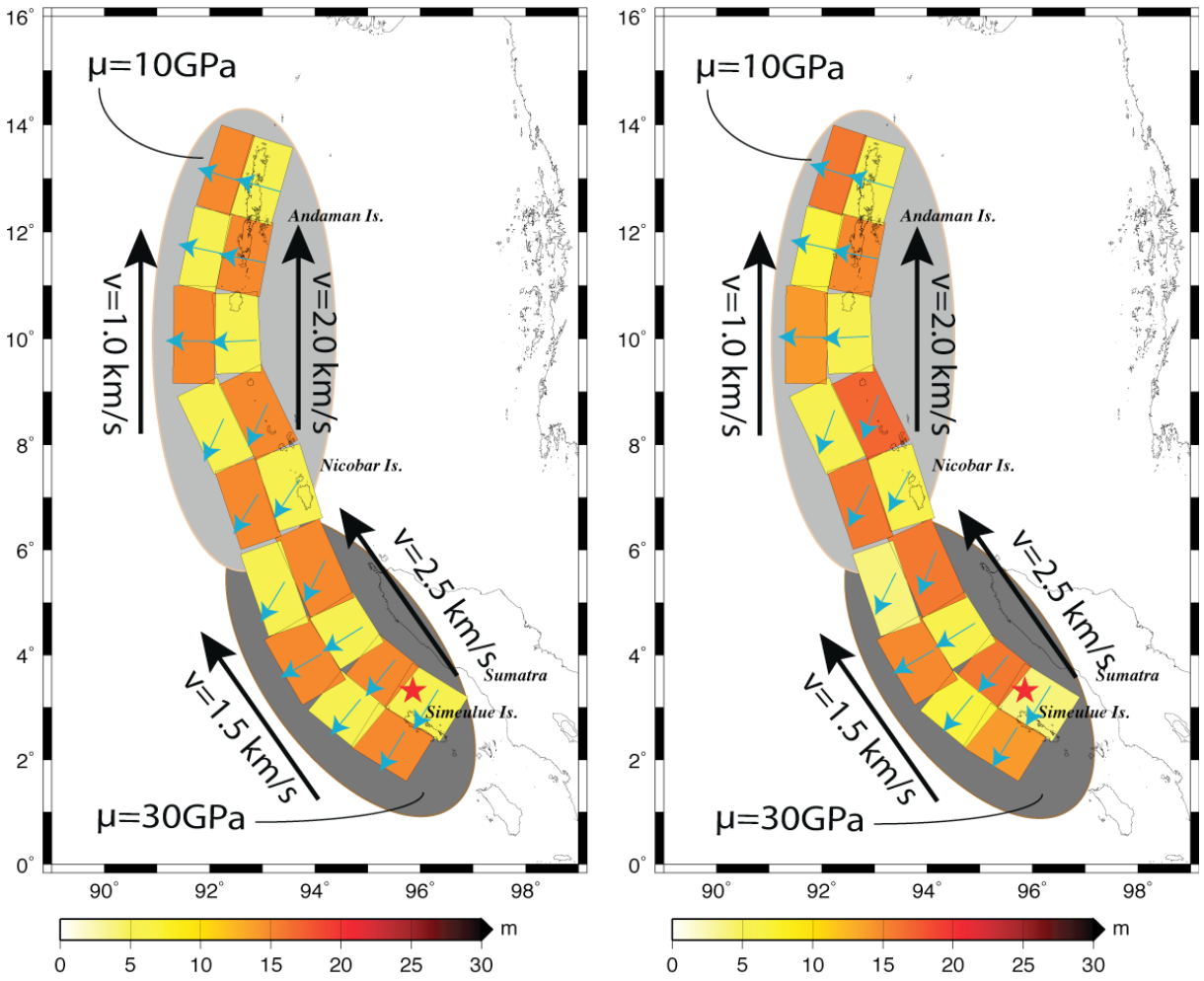
μ=10GPa
Andaman Is.
Nicobar Is.
v=1.0 km/s
v=2.0 km/s
v=2.5 km/s
Sumatra
Simeulue Is.
v=1.5 km/s
μ=30GPa
16°
14°
12°
10°
8°
6°
4°
2°
0°
90°
92°
94°
96°
98°
m
0
5
10
15
20
25
30

FIGURE 5

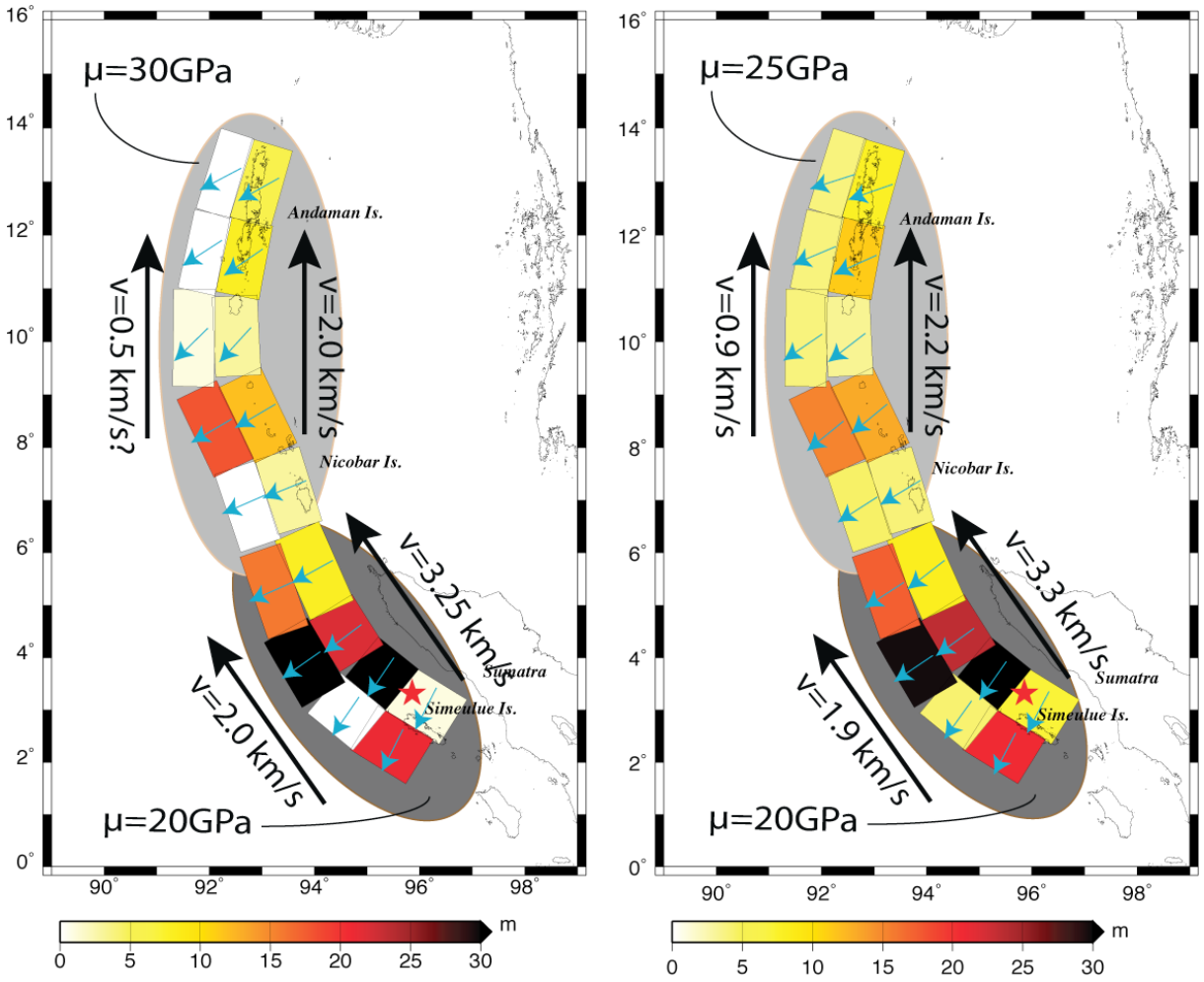
μ=30GPa
Andaman Is.
Nicobar Is.
Sumatra
Simeulue Is.
v=0.5 km/s?
v=2.0 km/s
v=3.25 km/s
v=2.0 km/s
μ=20GPa
μ=25GPa
Andaman Is.
Nicobar Is.
Sumatra
Simeulue Is.
v=0.9 km/s
v=2.2 km/s
v=3.3 km/s
v=1.9 km/s
μ=20GPa
16°
14°
12°
10°
8°
6°
4°
2°
0°
90°
92°
94°
96°
98°
m
0
5
10
15
20
25
30

FIGURE 6

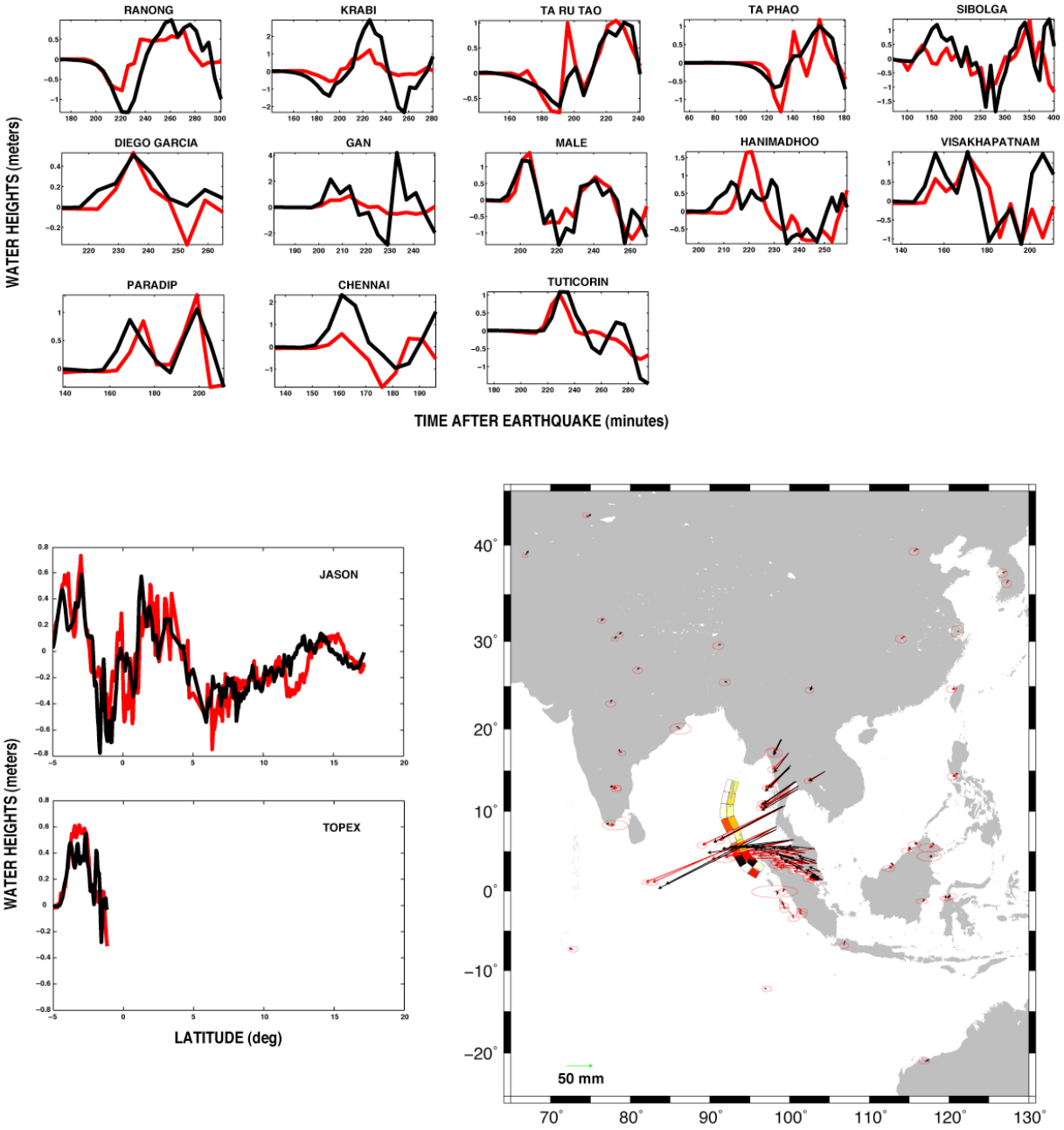
RANONG
KRABI
TA RU TAO
TA PHAO
SIBOLGA
DIEGO GARCIA
GAN
MALE
HANIMADHOO
VISAKHAPATNAM
PARADIP
CHENNAI
TUTICORIN
WATER HEIGHTS (meters)
TIME AFTER EARTHQUAKE (minutes)
JASON
TOPEX
WATER HEIGHTS (meters)
LATITUDE (deg)
50 mm

FIGURE 7

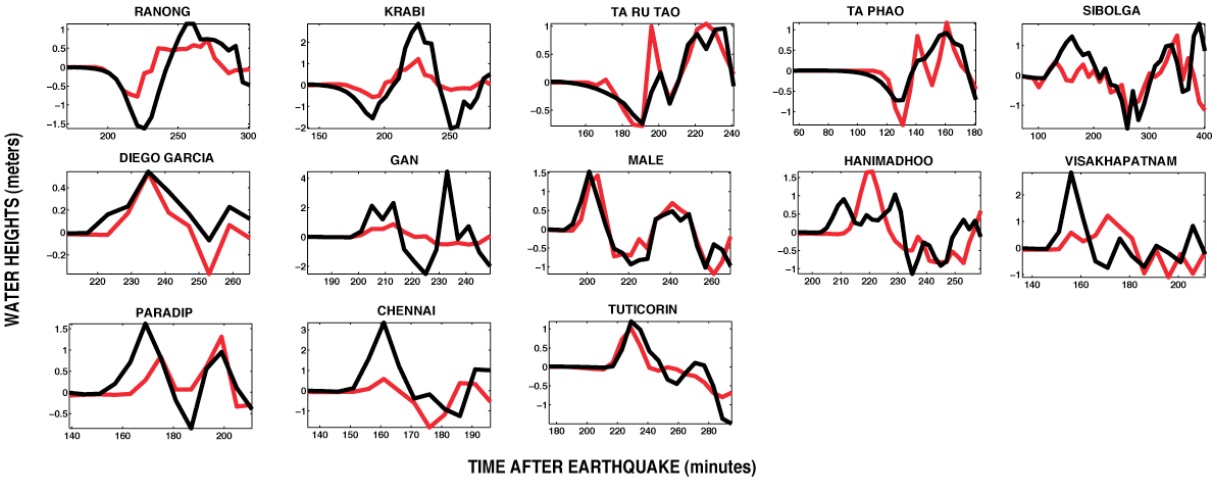
RANONG
KRABI
TA RU TAO
TA PHAO
SIBOLGA
DIEGO GARCIA
GAN
MALE
HANIMADHOO
VISAKHAPATNAM
PARADIP
CHENNAI
TUTICORIN
WATER HEIGHTS (meters)
TIME AFTER EARTHQUAKE (minutes)

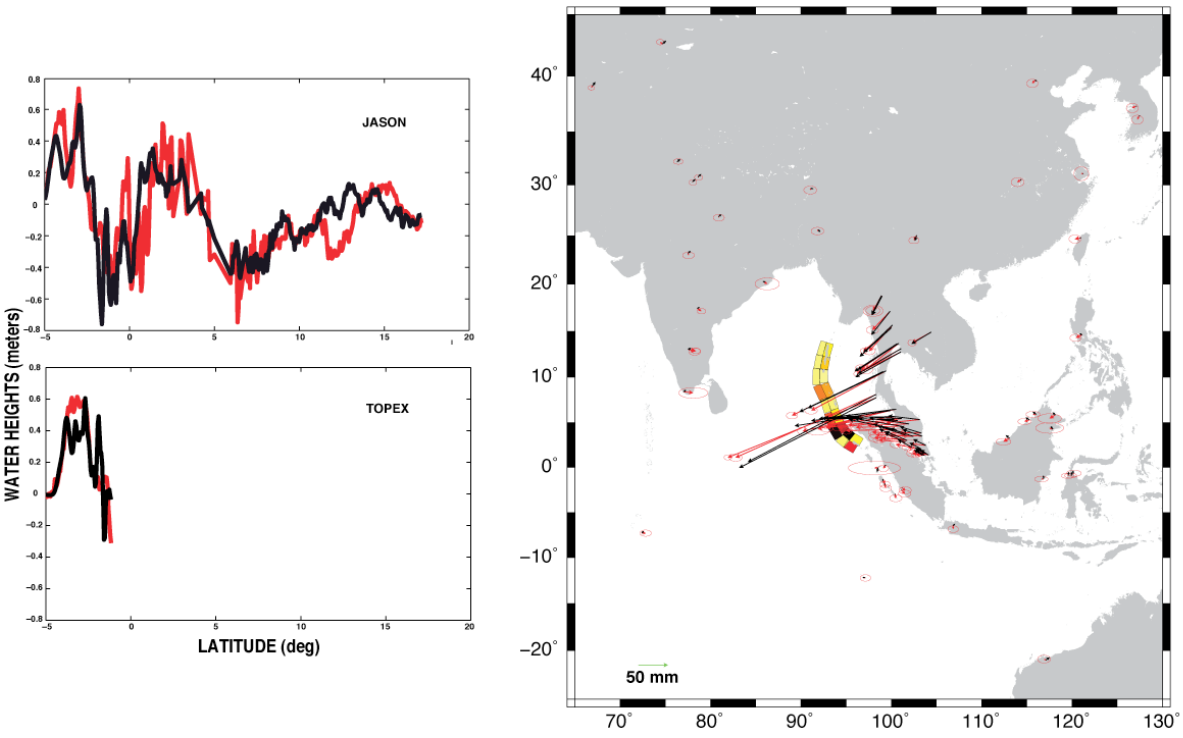
JASON
TOPEX
WATER HEIGHTS (meters)
LATITUDE (deg)
50 mm

FIGURE 8

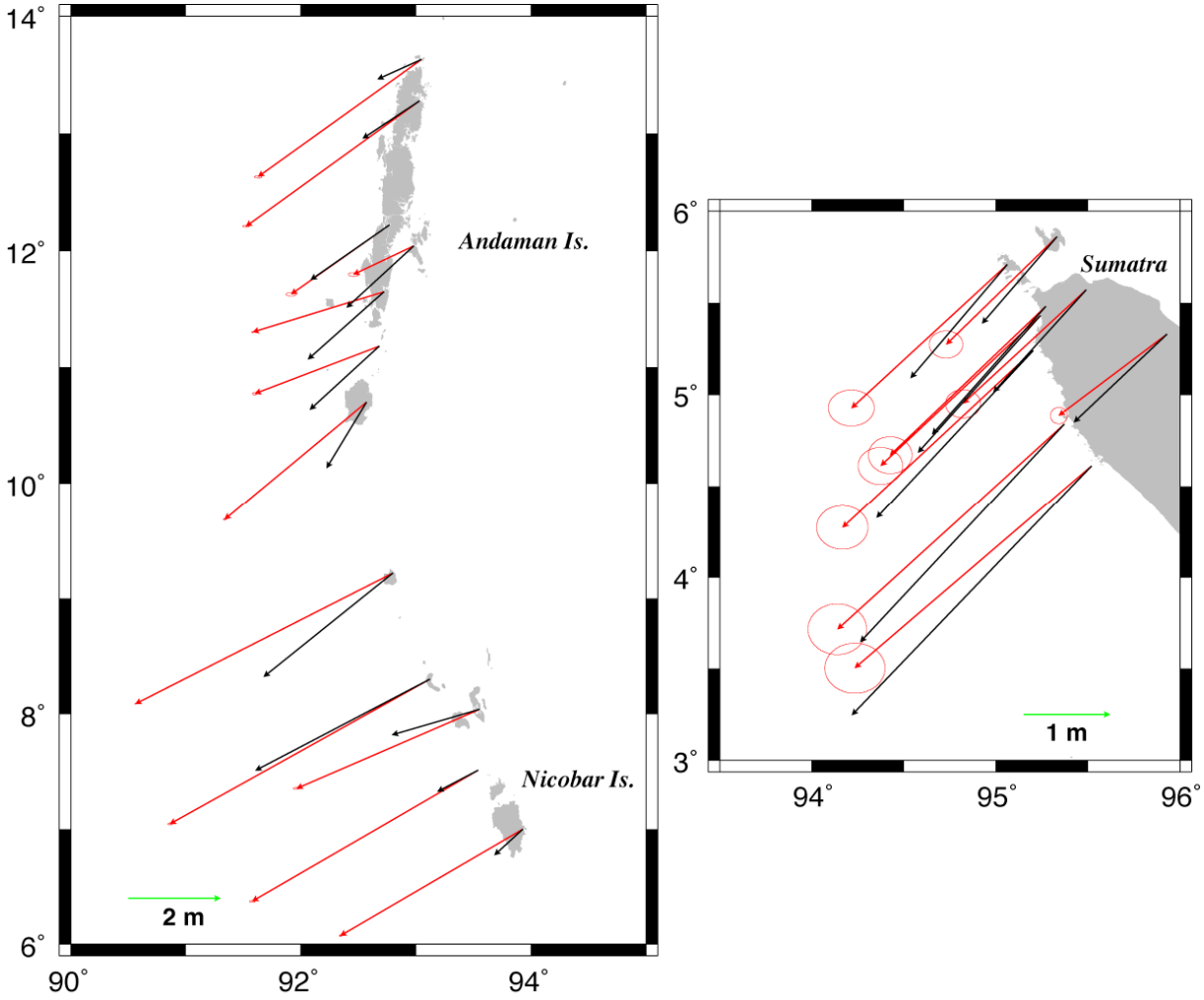
14°
12°
10°
8°
6°
90°
92°
94°
Andaman Is.
Nicobar Is.
2 m
6°
5°
4°
3°
94°
95°
96°
Sumatra
1 m

FIGURE 9

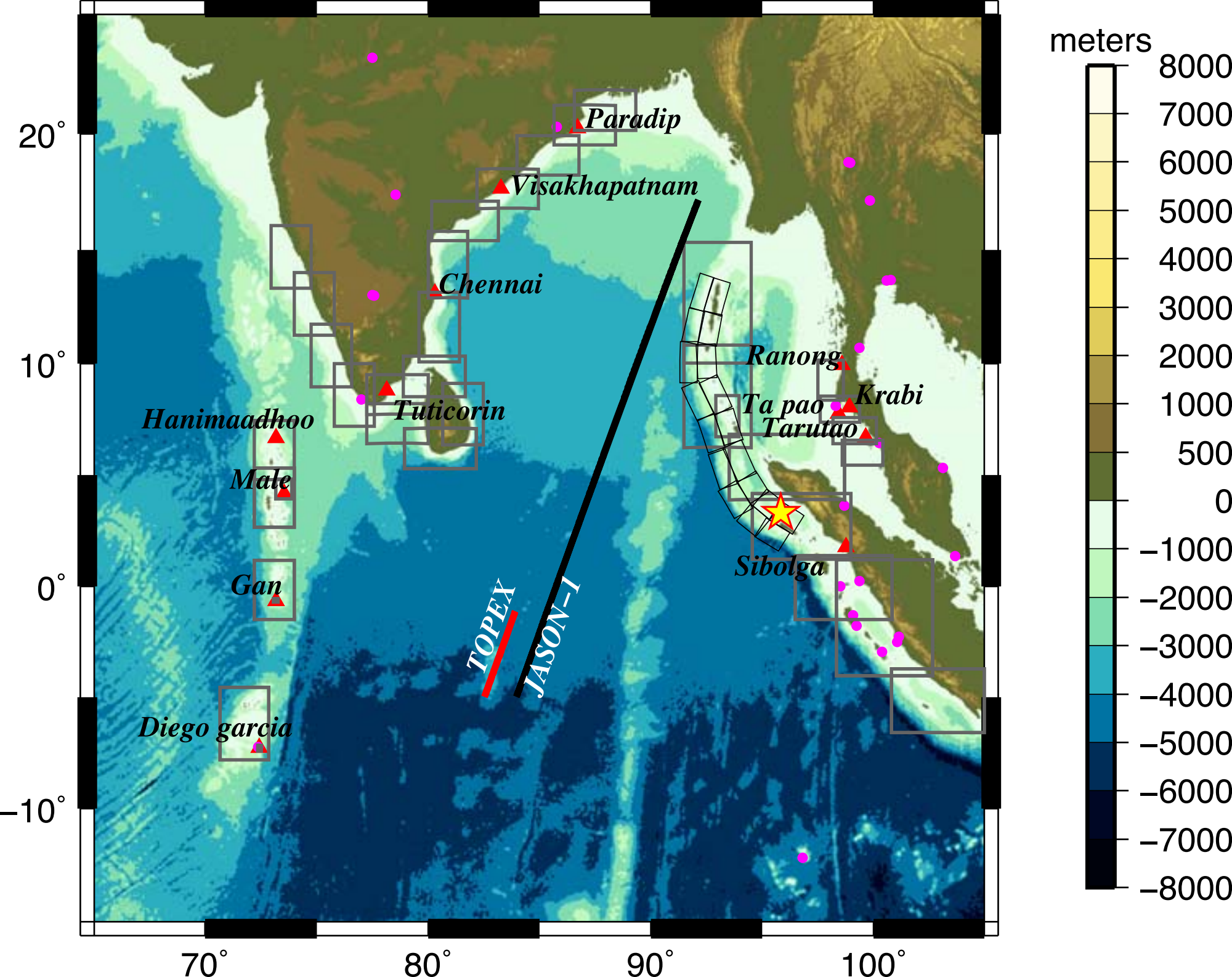
Paradip
Visakhapatnam
Chennai
Tuticorin
Hanimaadhoo
Male
Gan
Diego garcia
Ranong
Ta pao
Krabi
Tarutao
Sibolga
TOPEX
JASON-1
20°
10°
0°
−10°
70°
80°
90°
100°
meters
8000
7000
6000
5000
4000
3000
2000
1000
500
0
−1000
−2000
−3000
−4000
−5000
−6000
−7000
−8000

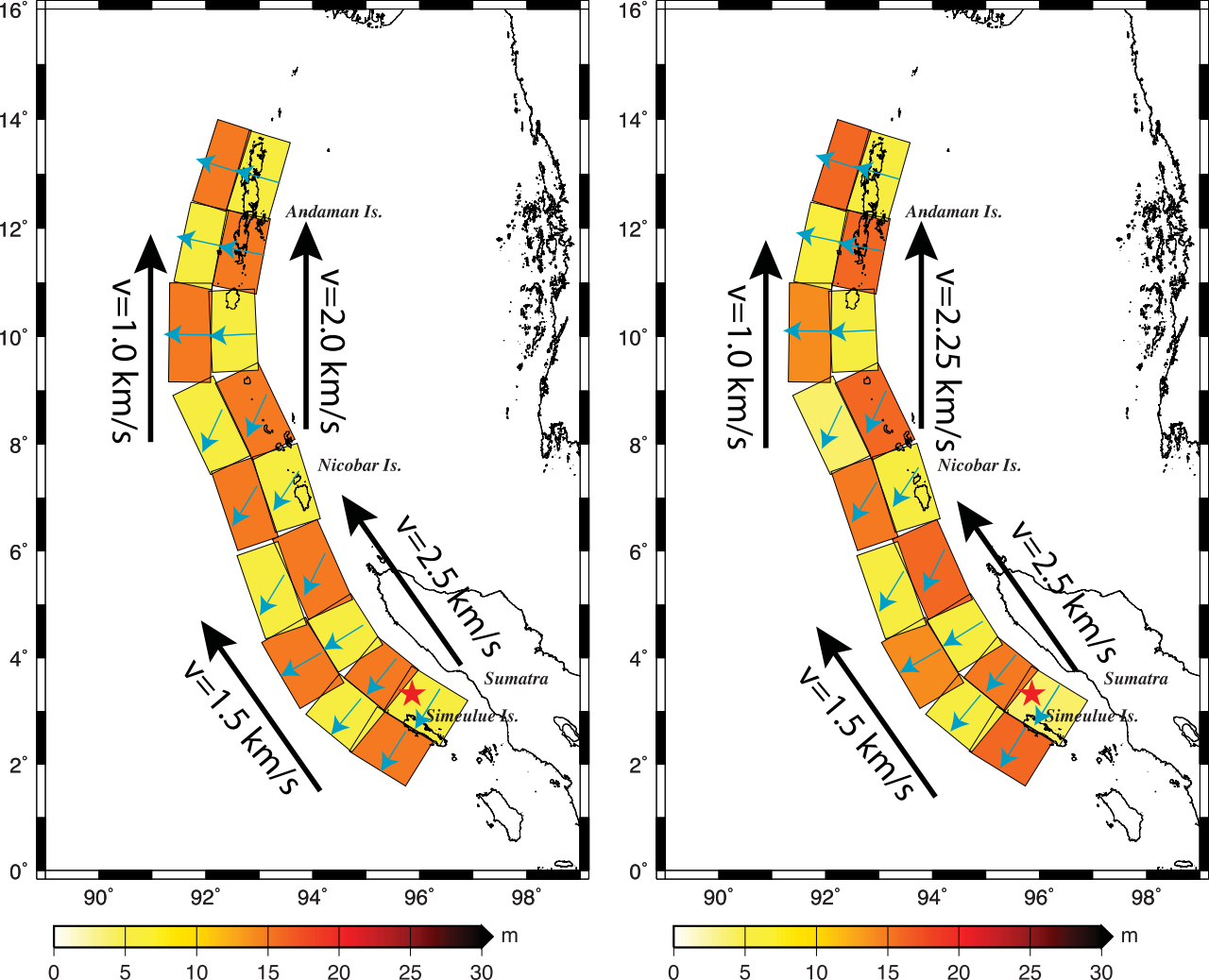
Andaman Is.
Nicobar Is.
Sumatra
Simeulue Is.
v=1.0 km/s
v=2.0 km/s
v=2.5 km/s
v=1.5 km/s
v=2.25 km/s
16°
14°
12°
10°
8°
6°
4°
2°
0°
90°
92°
94°
96°
98°
m
0
5
10
15
20
25
30

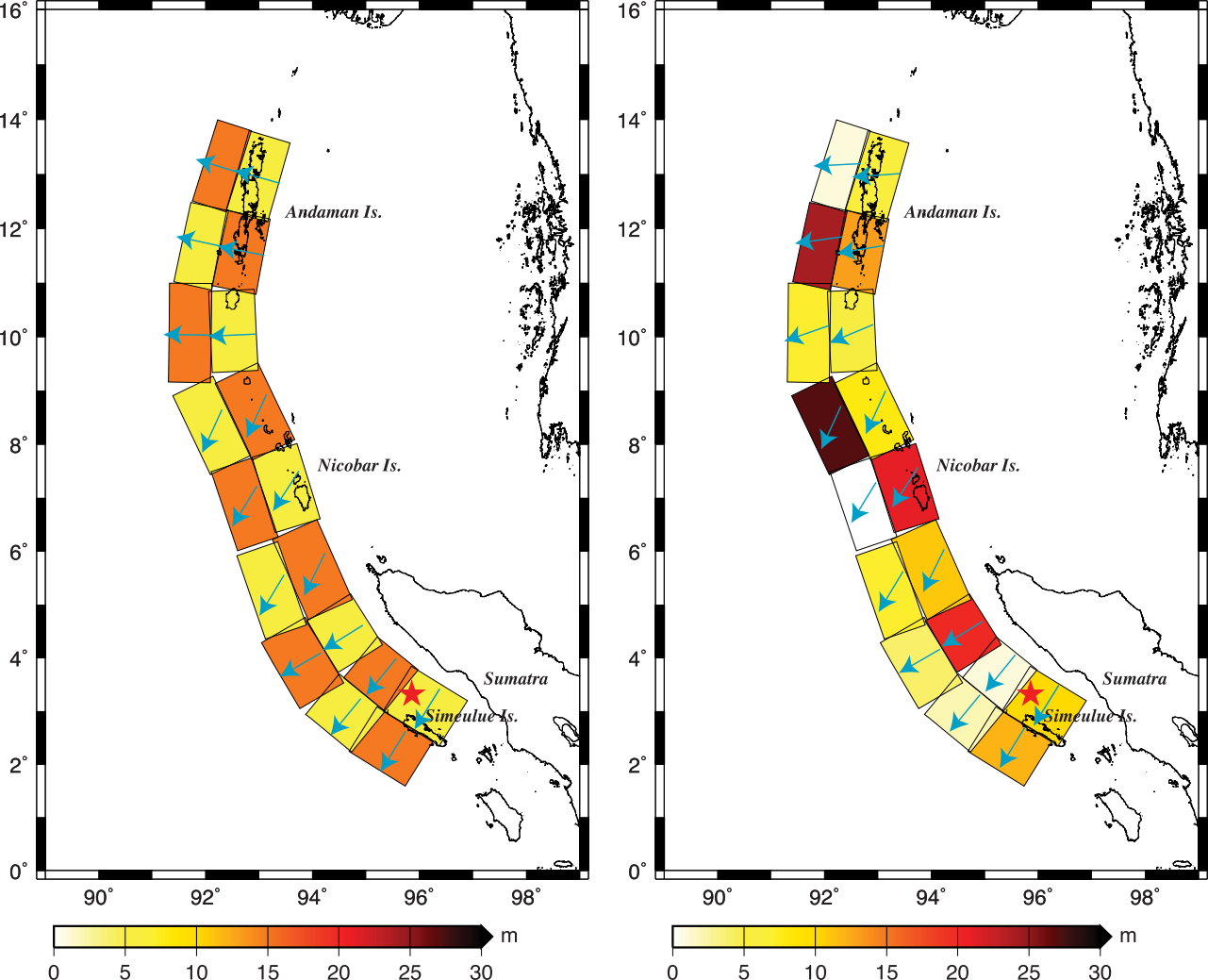
Andaman Is.
Nicobar Is.
Sumatra
Simeulue Is.
16°
14°
12°
10°
8°
6°
4°
2°
0°
90°
92°
94°
96°
98°
m
0
5
10
15
20
25
30

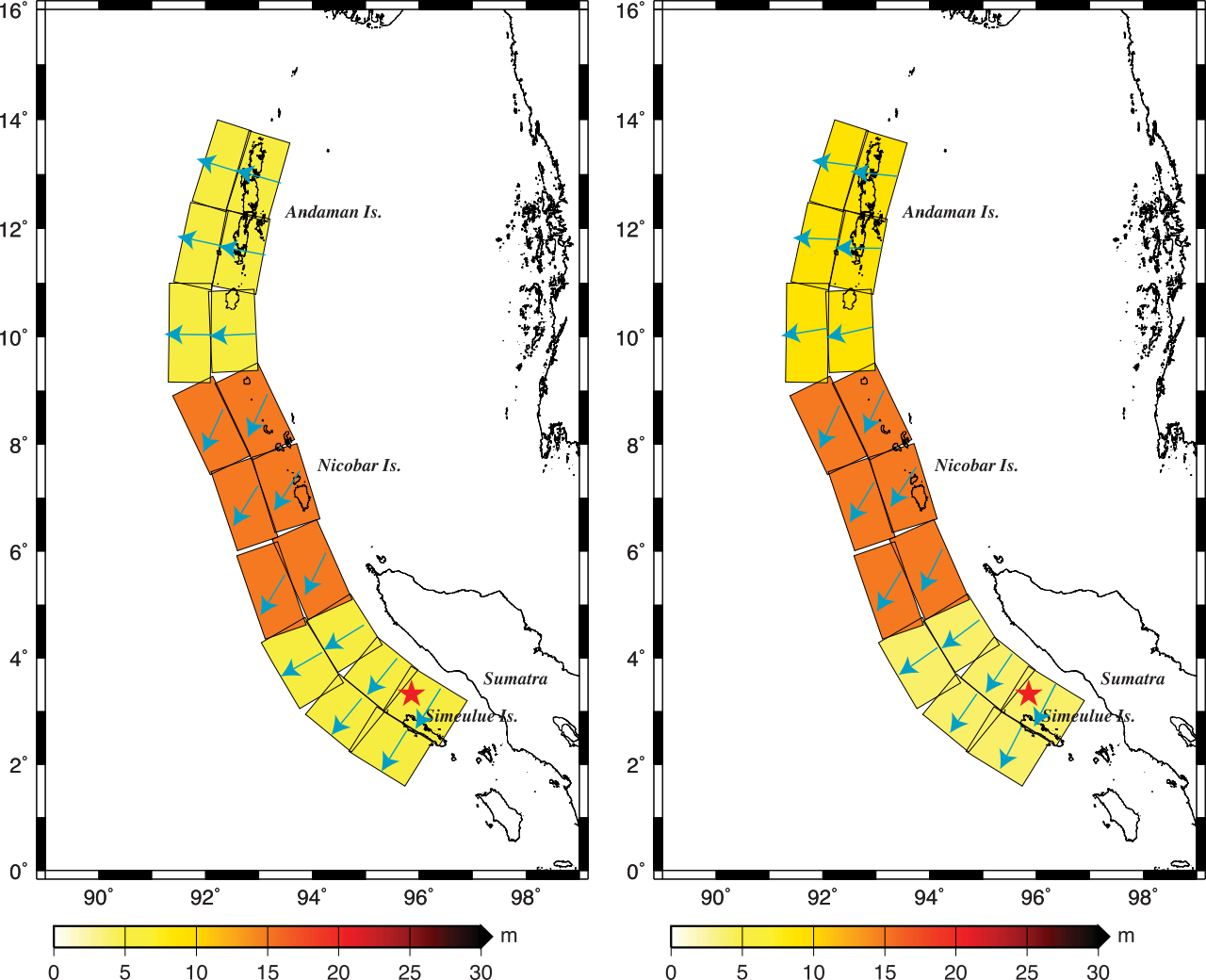
Andaman Is.
Nicobar Is.
Sumatra
Simeulue Is.
16°
14°
12°
10°
8°
6°
4°
2°
0°
90°
92°
94°
96°
98°
m
0
5
10
15
20
25
30

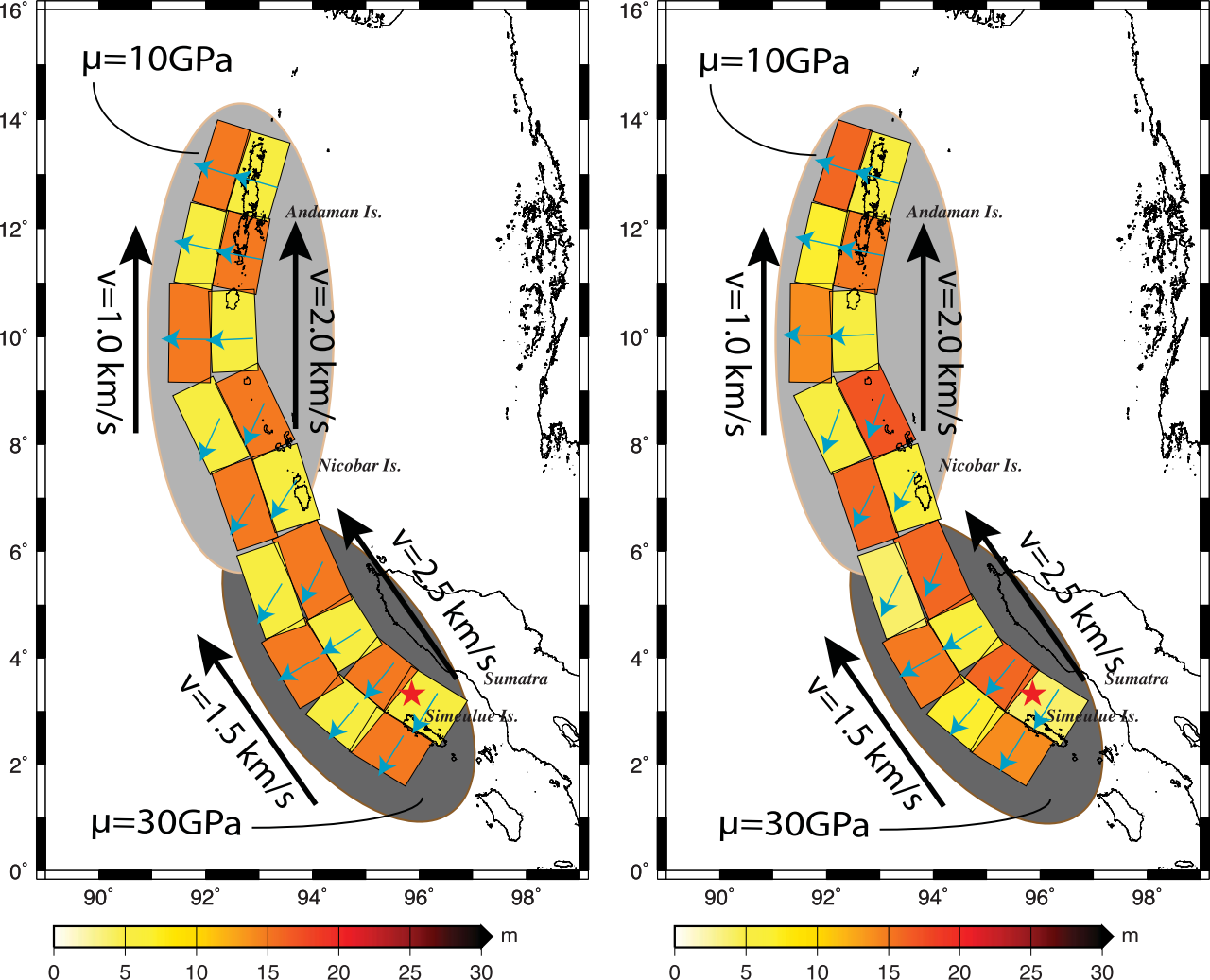
μ=10GPa
Andaman Is.
v=1.0 km/s
v=2.0 km/s
Nicobar Is.
v=2.5 km/s
Sumatra
Simeulue Is.
v=1.5 km/s
μ=30GPa
16°
14°
12°
10°
8°
6°
4°
2°
0°
90°
92°
94°
96°
98°
m
0
5
10
15
20
25
30

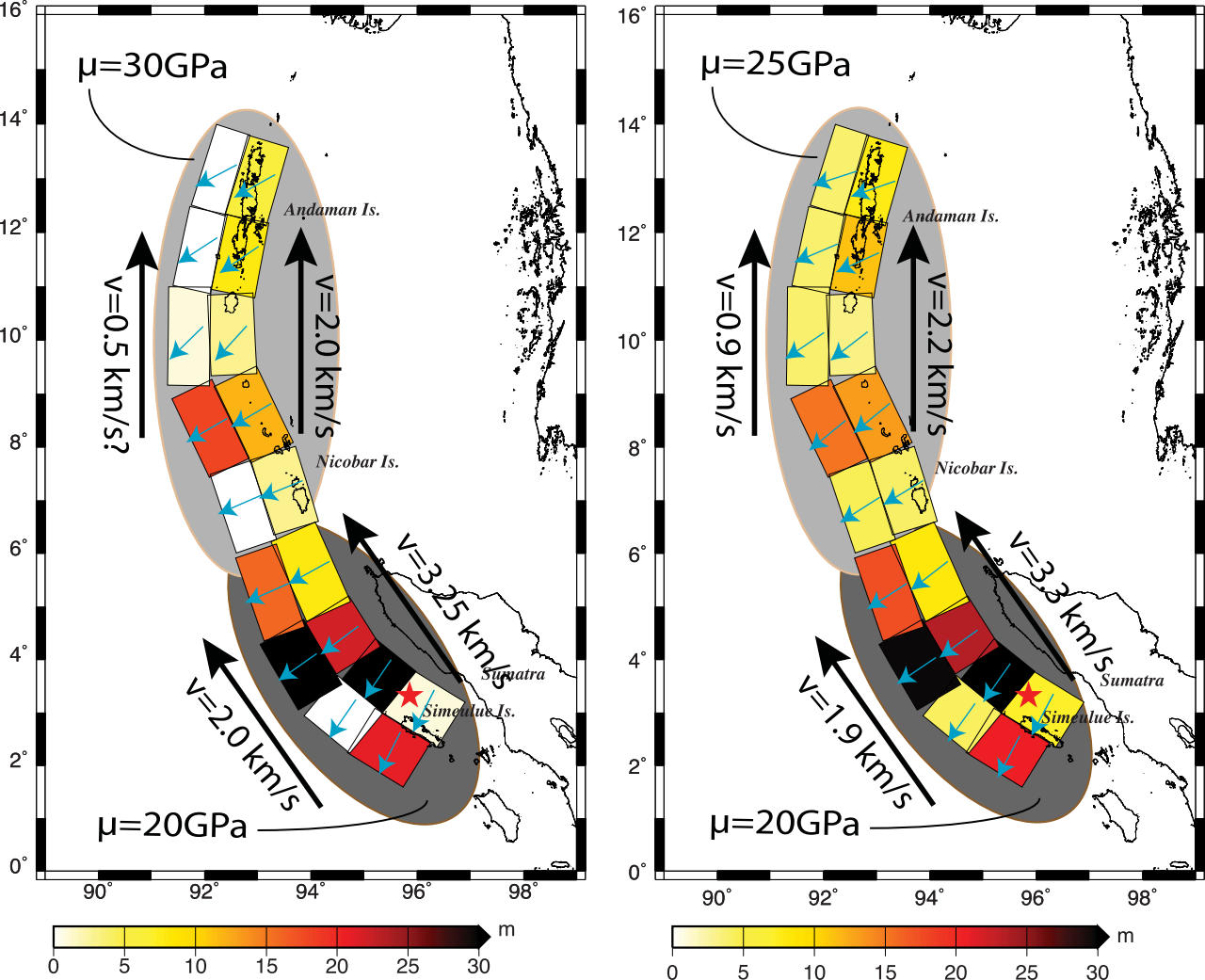
μ=30GPa
Andaman Is.
Nicobar Is.
Sumatra
Simeulue Is.
v=0.5 km/s?
v=2.0 km/s
v=3.25 km/s
v=2.0 km/s
μ=20GPa
μ=25GPa
Andaman Is.
Nicobar Is.
Sumatra
Simeulue Is.
v=0.9 km/s
v=2.2 km/s
v=3.3 km/s
v=1.9 km/s
μ=20GPa
16°
14°
12°
10°
8°
6°
4°
2°
0°
90°
92°
94°
96°
98°
m
0
5
10
15
20
25
30

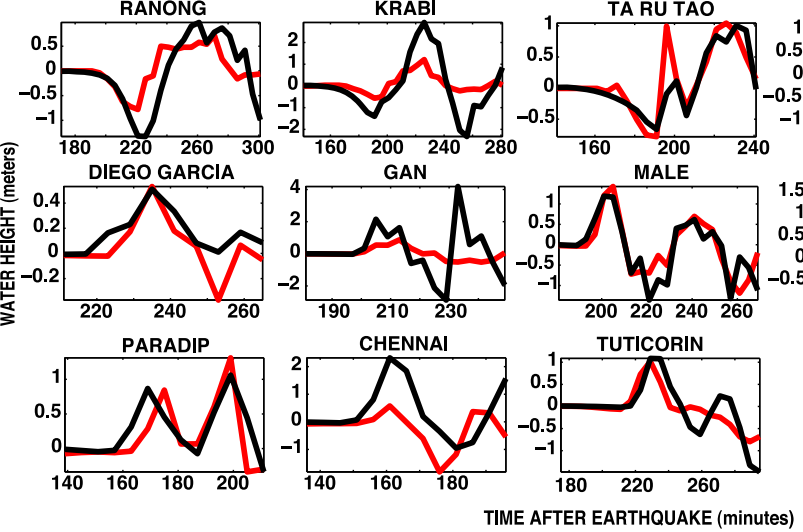
RANONG
KRABI
TA RU TAO
TA PHAO
SIBOLGA
DIEGO GARCIA
GAN
MALE
HANIMADHOO
VISAKHAPATNAM
PARADIP
CHENNAI
TUTICORIN
WATER HEIGHT (meters)
TIME AFTER EARTHQUAKE (minutes)

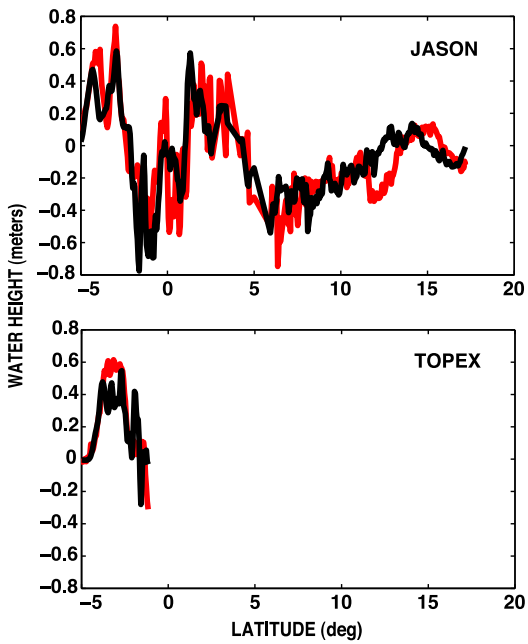
JASON
TOPEX
WATER HEIGHT (meters)
LATITUDE (deg)

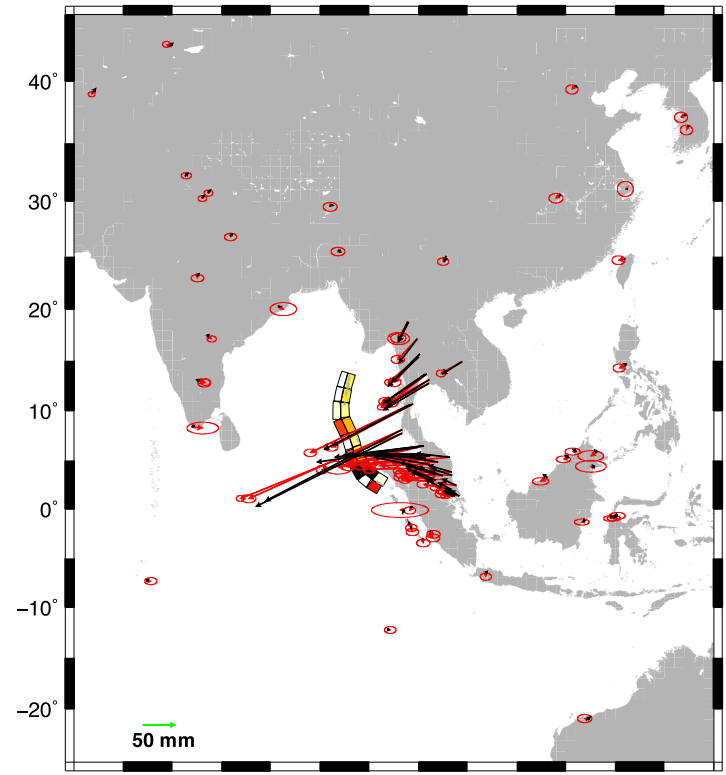
50 mm

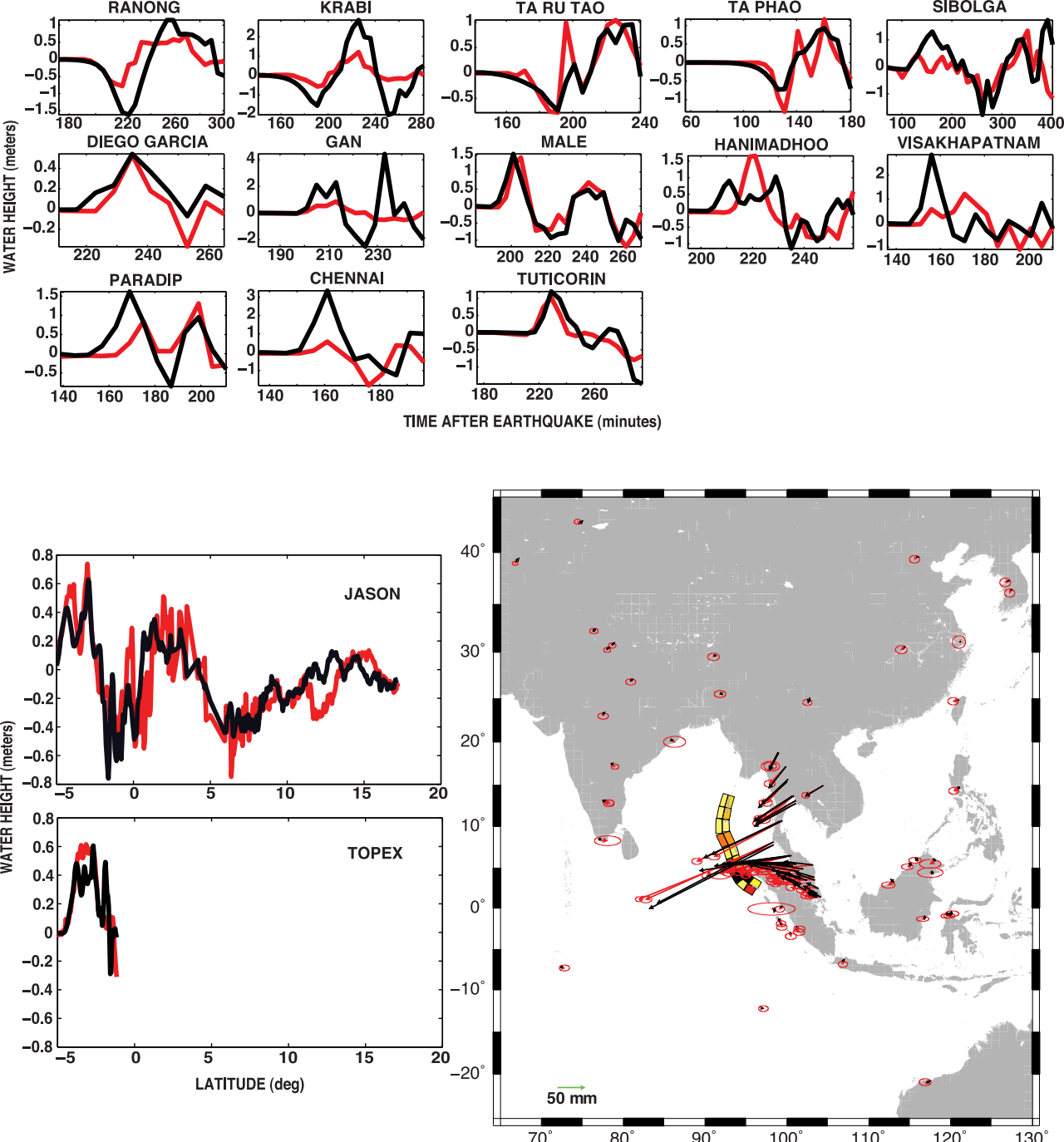
RANONG
KRABI
TA RU TAO
TA PHAO
SIBOLGA
DIEGO GARCIA
GAN
MALE
HANIMADHOO
VISAKHAPATNAM
PARADIP
CHENNAI
TUTICORIN
WATER HEIGHT (meters)
TIME AFTER EARTHQUAKE (minutes)
JASON
TOPEX
WATER HEIGHT (meters)
LATITUDE (deg)
50 mm

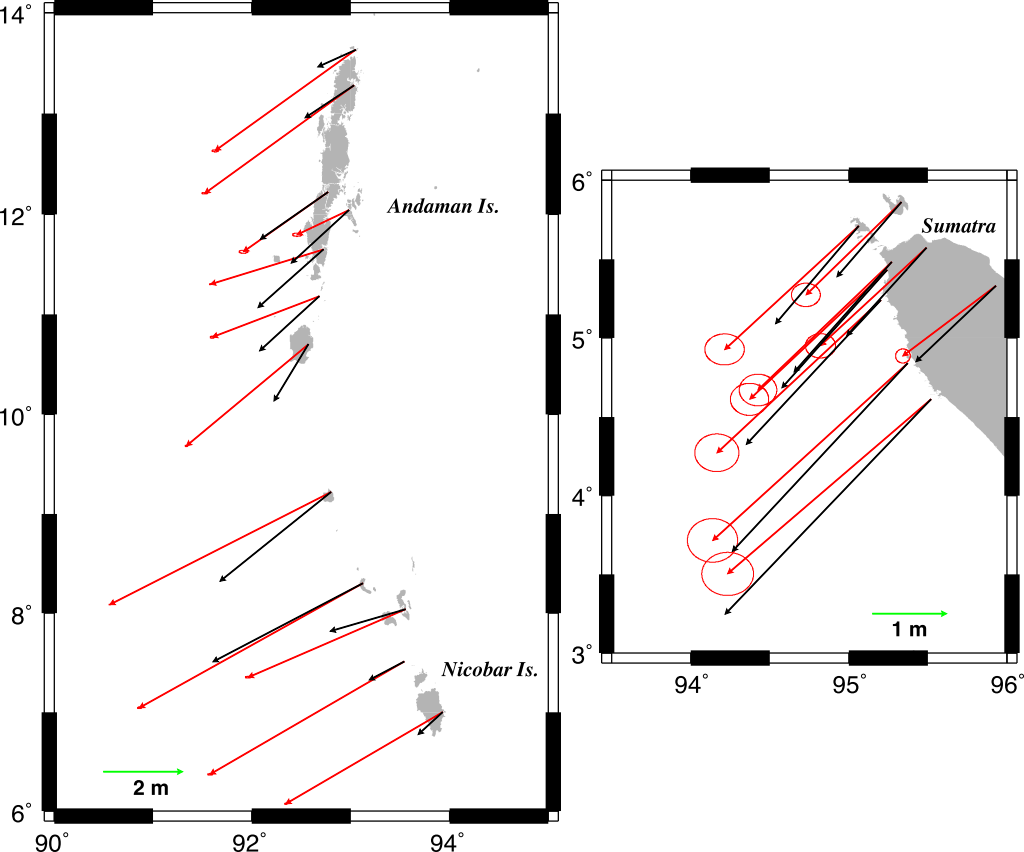
Andaman Is.
Nicobar Is.
Sumatra
2 m
1 m
14°
12°
10°
8°
6°
90°
92°
94°
6°
5°
4°
3°
94°
95°
96°